Spatial distribution of aerosol microphysical and optical properties and direct radiative effect from the China Aerosol Remote Sensing Network

Huizheng Che[1*], Xiangao Xia[2,3], Hujia Zhao[1,4], Oleg Dubovik[5], Brent N. Holben[6], Philippe Goloub[5], Emilio Cuevas-Agulló[7], Victor Estelles[8], Yaqiang Wang[1], Jun Zhu[9] Bing Qi[10], Wei Gong [11], Honglong Yang[12], Renjian Zhang[13], Leiku Yang[14], Jing Chen[15], Hong Wang[1], Yu Zheng[1], Ke Gui[1], Xiaochun Zhang[16], Xiaoye Zhang[1*]

1   State Key Laboratory of Severe Weather (LASW) and Key Laboratory of Atmospheric Chemistry (LAC), Chinese Academy of Meteorological Sciences, CMA, Beijing, 100081, China

2   Laboratory for Middle Atmosphere and Global Environment Observation (LAGEO), Institute of Atmospheric Physics, Chinese Academy of Sciences, Beijing, 100029, China

3   University of Chinese Academy of Science, Beijing, 100049, China

4   Institute of Atmospheric Environment, CMA, Shenyang, 110016, China

5   Laboratoire d'Optique Amosphérique, Université des Sciences et Technologies de Lille, 59655, Villeneuve d'Ascq, France

6   NASA Goddard Space Flight Center, Greenbelt, MD, USA

7   Centro de Investigación Atmosférica de Izaña, AEMET, 38001 Santa Cruz de Tenerife , Spain

8   Dept. Fisica de la Terra i Termodinamica, Universitat de Valencia, C/ Dr. Moliner 50, 46100 Burjassot, Spain

9   Collaborative Innovation Center on Forecast and Evaluation of Meteorological Disasters, Nanjing University of Information Science & Technology, Nanjing, 210044, China

10   Hangzhou Meteorological Bureau, Hangzhou, 310051, China

11   State Key Laboratory of Information Engineering in Surveying, Mapping and Remote Sensing, Wuhan University, Wuhan, 430079, China

12   Shenzhen Meteorological Bureau, Shenzhen, 518040, China

13   Key Laboratory of Regional Climate-Environment Research for Temperate East Asia, Institute of Atmospheric Physics, Beijing, 100029, Chinese Academy of Sciences.

14   School of Surveying and Land Information Engineering, Henan Polytechnic University, Jiaozuo, 454000, China

15   Shijiazhuang Meteorological Bureau, Shijiazhuang, 050081, China

16   Meteorological Observation Center, CMA, Beijing, 100081

Corresponding author: chehz@cma.gov.cn & xiaoye@cma.gov.cn

Abstract

Multi-year observations of aerosol microphysical and optical properties obtained through ground-based remote sensing at 50 China Aerosol Remote Sensing Network (CARSNET) sites were used to characterize the aerosol climatology for representative remote, rural, and urban areas over China to assess effects on climate. The annual mean effective radii for total particles (R_{efft}) decreased from north to south and from rural to urban sites, and high total particle volumes were found at the urban sites. The aerosol optical depth at 440 nm (AOD_{440nm}) increased from remote/rural sites (0.12) to urban sites (0.79), and the extinction Ångström exponent ($EAE_{440-870nm}$) increased from 0.71 at the arid/semi-arid sites to 1.15 at the urban sites, presumably due to anthropogenic emissions. Single scattering albedos ($SSA_{440\,nm}$) ranged from 0.88 to 0.92 indicating slightly to strongly absorbing aerosols. Absorption AOD_{440nm}'s were 0.01 at the remote sites versus 0.07 at the urban sites. The average direct aerosol radiative effect (DARE) at the bottom of atmosphere increased from the sites in the remote (-24.40 W/m^2) to the urban area (-103.28 W/m^2) indicating increased cooling at the latter. The DARE for the top of the atmosphere increased from -4.79 W/m^2 at the remote sites to -30.05 W/m^2 at the urban sites, indicating overall cooling effects for the earth-atmosphere system. A classification method based on $SSA_{440\,nm}$, fine mode fraction (FMF), and $EAE_{440-870\,nm}$ showed that coarse mode particles (mainly dust) were dominant at the rural sites near the northwestern deserts, while light-absorbing, fine-mode particles were important at most urban sites. This study will be important for understanding aerosol climate effects and regional environmental pollution, and the results will provide useful information for satellite validation and the improvement of climate modeling.

Keywords: aerosol optical properties; direct aerosol radiative effect; aerosol type; climatology; China Aerosol Remote Sensing Network

1. Introduction

Atmospheric aerosols have important direct effects on climate because they can scatter and absorb radiant energy and in so doing affect the Earth's energy balance (Charlson et al., 1992; Yang et al., 2016). Meanwhile, the aerosols can be served as cloud condensation nuclei or ice nuclei to affect the climate indirectly through aerosol–cloud interactions (Twomey et al., 1984; Garrett et al., 2006; Zhao et al., 2015; Xie et al., 2013). The optical properties of the aerosol determine the particles' direct effects on the Earth's radiative balance and weather-climate change (Ramanathan et al., 2001; Eck et al., 2005; Myhre, 2009; Zhao et al., 2018). Aerosol optical depth (AOD) is one of the key measures of the total aerosol extinction effects on climate (Breon et al., 2002), and the extinction Ångström exponent (EAE) with spectral dependence can be used to obtain the information about aerosol size distributions (Gobbi et al., 2007; Eck et al., 1999; Zheng et al., 2017). The aerosols' absorptivity depends on particle composition is a key determinant to calculate the direct aerosol radiative effect (Haywood and Shine, 1995; Li et al., 2016; Zheng et al., 2018), and the single scattering albedo (SSA) is the parameter has spectral dependence to distinguish major aerosol particle types (Jacobson et al., 2000; Dubovik et al., 2002; Gelencser et al., 2004; Russell et al., 2010; Giles et al., 2012).

With the recognition of the importance for climate, the aerosol optical properties have been obtained from ground-based monitoring networks worldwide; some of the major networks include AERONET-Aerosol Robotic Network (Holben et al., 1998) and its sub-networks of PHOTONS-PHOtométrie pour le Traitement Opérationnel de Normalisation Satellitaire, AEROCAN-Canadian Sun-Photometer Network, and RIMA-Iberian Network for aerosol measurements (Goloub et al., 2007; Bokoye et al., 2001; Prats et al., 2011), SKYNET-SKYrad Network (Takamura and Nakajima, 2004; Che et al., 2008), EARLINET-European aerosol Lidar network (Pappalardo et al., 2014), the GAW-PFR Network-Global Atmosphere Watch

Programmer-Precision Filter Radiometers (Wehrli, 2002; Estellés et al., 2012),. The CARSNET-China Aerosol Remote Sensing NETwork, the CSHNET-Chinese Sun Hazemeter Network and the SONET-Sun–Sky Radiometer Observation Network have been established to measure aerosol optical properties in China (Che et al., 2009a, 2015; Xin et al., 2007; Li et al., 2018). Furthermore, the aerosol optical properties have also been used in comprehensive studies of aerosol physical characteristics and chemical composition in many regions of China (Che et al., 2009c, 2018; Zhao et al., 2018).

China has become one of the largest aerosol sources in the world associated with its rapid economic development, and this has caused significant effects on local environments and regional climate (Che et al., 2005; Xia, 2010; Li et al., 2016; Yang et al., 2018, 2019; Zhao et al., 2019). There have been numerous studies that have focused on aerosol optical properties obtained though ground-based remote sensing methods in China (Luo et al., 2002; Li et al., 2003; Duan and Mao, 2007). A few researches have paid more attention to the aerosol optical properties and its radiative effects over the urban-industrial areas as well as at coastal sites in northeastern and eastern China (Wang et al., 2010; Xin et al., 2011; Xia et al., 2007; Zhao et al., 2016; Wu et al. 2012; Shen et al., 2019). Many studies of aerosol optical properties were conducted in northern China with high aerosol loadings, such as the Beijing-Tianjin-Hebei region (Che et al. 2014; Xia et al., 2013; Fan et al., 2006; Xie et al., 2008; Zhang et al., 2019; Yang et al., 2019; Zhao et al., 2018). Aerosol optical properties also have been investigated at Hefei, Shouxian, Nanjing, Taihu, Shanghai and other sites in eastern China (Lee et al., 2010; He et al., 2012; Zhuang et al., 2014; Wang Z et al., 2015; Che et al., 2018). Some studies of aerosol optical properties have been made in southern China (Wang et al., 2015; Tao et al., 2014), and those at remote and rural sites in China provide information on regional background conditions (Che et al., 2009b; Wang et al., 2010; Xue et al., 2011; Zhu et al., 2014; Yuan et al., 2014).

China's vast size, varied terrain, and heterogeneity of aerosol sources, has led to strong temporal and spatial variability in aerosol optical and physical properties. The mixtures of aerosol types at most sites are complex, and aerosol populations' size and composition are affected by their sources, transformations that occurring during transportation and removing processes (Cao et al., 2007; Wang et al., 2007; Zhang et al., 2013; Wan et al., 2015). National scale, ground-based measurements of aerosol microphysical and its optical properties obtained from the sunphotometer provide for a better understanding of the aerosols' climate effects over the different regions of China. The measurements of greatest interest include aerosol size distributions (volume and aerosol effective radii), optical properties (AOD, AE, SSA, absorption AOD) because those data can at least be used to evaluate aerosol direct radiative effect.

The aim of this study was focused on the investigation of the climatological spatial distribution of aerosol microphysical and optical properties over regional-scales using spatial distribution data from the national CARSNET network. The data were collected at CARSNET sites, which include sites in the remote, rural and urban area, with the same calibration procedures and calculation algorithms were used at all sites. As a result, the data are directly comparable among sites (Che et al., 2009a), and the results can be provided to characterize the regional distribution and temporal variation of aerosol optical properties. This research focused on aerosol climate effects and regional environmental pollution, and the results should be useful for satellite validations and for the improvement of models in the future. The remainder of this paper is organized as following: Section 2 firstly describes the sites in detail, and then introduced the methods in data processing of the aerosol optical properties as well as the direct aerosol radiative effect calculation through the retrieved aerosol optical parameters. Section 3 illustrates the aerosol microphysical and optical properties, as well as its direct aerosol radiative effect. An aerosol type classification method is proposed

according to the aerosol optical parameters. Section 4 presents the conclusions of the study.

2 Site description, instruments, and data

2.1 Site description

Sunphotometers (CE-318, Cimel Electronique, Paris, France, see Appendix A) were installed at 50 CARSNET sites (Fig. 1) from 2010 to 2017. The stations were classified as remote, rural, or urban sites based on administrative division (Appendix Table 1). Three of the remote stations were about more than 3000 m above the sea level on the Tibetan Plateau far from the anthropogenic influences, and one of them was a northwestern regional background site in China. The 23 rural sites represent (a) 5 sites of desert regions affected by most of dust aerosols rather than anthropogenic particles, (b) 2 sites affected by both dust and anthropogenic activities on the Loess Plateau, and (c) 16 sites located near or surrounding the large cities relatively strong to the impacts of anthropogenic activities in the central and eastern China. The last category is 24 urban sites located in provincial capitals or heavily populated cities.

2.2 Instruments and calibration

The CE-318 sunphotometers used in this study were calibrated annually, using the CARSNET calibration protocol, to verify the accuracy and reliability of the sky irradiance measurements (Holben et al., 1998; Che et al., 2009; Tao et al., 2014). The reference instruments for CARSNET were periodically calibrated at Izaña, Tenerife, Spain located at 28.31 °N, 16.50 °W (2391.0 m a.s.l.) in conjunction with the AERONET program. There are several different types of the Cimel instruments that have been used at the 50 sites in this network as follows: (1) logical type CE-318 sunphotometers (440 nm, 675 nm, 870 nm, 940 nm, 1020 nm and three 870 nm at the polarization band), (2) numerical type CE-318 sunphotometers (440 nm, 675 nm, 870 nm, 940 nm, 1020 nm and three polarization bands at 870 nm), (3) numerical type CE-318 sunphotometers at eight wavelengths (340 nm, 380 nm, 440 nm, 500 nm, 675

nm, 870 nm, 940 nm, and 1020 nm), (4) and numerical type CE-318 sunphotometers at nine wavelengths (340 nm, 380 nm, 440 nm, 500 nm, 675 nm, 870 nm, 940 nm, 1020 nm and 1640 nm).

Measurements used to retrieve AODs were at 340 nm, 380 nm, 440 nm, 500 nm, 675 nm, 870 nm, 1020 nm, and 1640 nm, while the total precipitable water content was obtained by using those measurements at 940 nm (Holben et al., 1998; Dubovik and King, 2000). The cloud-screened AOD data were calculated by using the ASTPwin software, and extinction Ångström exponents (EAE) were calculated from the instantaneous AODs for wavelengths of 440 nm and 870 nm (Che et al., 2009, 2015). Sites with more than three daily AOD observations and more than 10 monthly AOD observation days were used to calculate the daily and monthly mean AODs and extinction Ångström exponents. The FMF is described as the fraction of fine mode particles of total AOD_{440nm} ($AOD_{fine440\ nm}/AOD_{440\ nm}$).

2.3. Data processing

The aerosol microphysical and optical properties, including volume size distributions (dV(r)/dlnr), the total, fine, and coarse mode aerosol effective radii (R_{effT}, R_{effF}, and R_{effC}, respectively) single-scattering albedo (SSA), complex refractive indices, absorption AODs (AAODs), and absorption Ångström exponents (AAEs), were retrieved from the observational data from the sky scattering channel of the sunphotometers at 440 nm, 670 nm, 870 nm, 1020 nm using the algorithms of Dubovik et al. (2002, 2006). In the process of retrieval, the data of surface albedo (SA) was interpolated or extrapolated to 440 nm, 670 nm, 870 nm, and 1020 nm based on the daily MCD43C3 data, a product from the MODIS-Moderate Resolution Imaging Spectroradiometer surface reflectance (https://ladsweb.modaps.eosdis.nasa.gov/). The algorithm used to calculate aerosol volume size distributions (dV(r)/dlnr) was under the assumption of a homogeneous distribution of non-spherical particles following the approach of Dubovik (2006). The sphericity fraction retrieved from the

216 inversions is defined as: spherical particles/(spheroidal particles + spherical

217 particles) (Giles et al., 2011).

218 As Dubovik et al. (2002, 2006) defined that all the particles with effective

219 radii < 0.992 μm were considered as fine mode particles; and those > 0.992

220 μm were considered as coarse mode particles. For the total (R_{effT}), fine (R_{effF})

221 and coarse (R_{effC}) mode aerosols, the effective radii are calculated by the

222 equation as follows:

223
$$R_{eff} = \frac{\int_{r_{min}}^{r_{max}} r^3 \frac{dN(r)}{dlnr} dlnr}{\int_{r_{min}}^{r_{max}} r^2 \frac{dN(r)}{dlnr} dlnr} \qquad (1)$$

224 Where r_{min} denotes 0.05, 0.05, 0.992 μm and r_{max} denotes 15, 0.992, 15

225 μm of the total, fine and coarse mode particles, respectively.

226 The coarse (PV_C) and fine aerosol particle volumes distributions (PV_F) are

227 calculated according to a bimodal lognormal function descript by Whitby

228 (1978), Shettle and Fenn (1979) and Remer and Kaufman (1998):

229
$$\frac{dV(r)}{dlnr} = \sum_{i=1}^{2} \frac{C_{v,i}}{\sqrt{2\pi}\sigma_i} exp\left[-\frac{(lnr - lnr_{V,i})^2}{2\sigma_i^2}\right] \qquad (2)$$

230 where $C_{v,i}$ means for the volume concentration; $r_{V,i}$ means the median

231 radius, and σ_i means the standard deviation.

232 The volume median radius is computed by fine and coarse modes

233 particles as follows:

234
$$lnr_V = \frac{\int_{r_{min}}^{r_{max}} lnr \frac{dV(r)}{dlnr} dlnr}{\int_{r_{min}}^{r_{max}} \frac{dV(r)}{dlnr} dlnr} \qquad (3)$$

235 Then the standard deviation is calculated from the volume median radius:

236
$$\sigma_V = \sqrt{\frac{\int_{r_{min}}^{r_{max}} (lnr - lnr_V)^2 \frac{dV(r)}{d lnr} d lnr}{\int_{r_{min}}^{r_{max}} \frac{dV(r)}{d lnr} d lnr}} \qquad (4)$$

The volume concentration ($\mu m^3/\mu m^2$) is speculated by the following equation:

$$C_V = \int_{r_{min}}^{r_{max}} \frac{dV(r)}{d\,lnr} d\,lnr \qquad (5)$$

The SSA was retrieved only for $AOD_{440nm} > 0.40$; this was done to avoid the larger uncertainty inherent in the lower AOD retrieval according to Dubovik et al. (2002, 2006). The AAOD and AAE for wavelength λ were calculated as follows:

$$AAOD(\lambda) = [1 - SSA(\lambda)] \times AOD(\lambda) \qquad (6)$$

$$AAE = \frac{-dln[AAOD(\lambda)]}{dln(\lambda)} \qquad (7)$$

The total AODs' uncertainty was 0.01 to 0.02 according to Eck et al. (1999). The accuracy of SSA retrieved from $AOD_{440nm} > 0.50$ with solar zenith angles > 50 was 0.03 (Dubovik et al., 2002). The accuracy of the particle volume size distribution was 15–25% between $0.1\ \mu m \le r \le 7.0\ \mu m$ and 25–100% in conditions of $r < 0.1\ \mu m$ and $r > 7\mu m$.

Direct aerosol radiative effect (DARE in W/m^2) was calculated by the radiative transfer module under cloud-free conditions, which is similar to the inversion of AERONET (García et al., 2008; 2012). The DARE at the bottom of the atmosphere (BOA) and the top of the atmosphere (TOA) was defined as the difference in the shortwave radiative fluxes with and without aerosol effects as follows:

$$DARE_{TOA} = F_{TOA}^{\uparrow 0} - F_{TOA}^{\uparrow} \qquad (8)$$

$$DARE_{BOA} = F_{BOA}^{\downarrow} - F_{BOA}^{\downarrow 0} \qquad (9)$$

Where F and F^0 denoted the broadband fluxes of including and excluding

263 aerosols, respectively at the BOA and TOA. The " ↑ " and " ↓ "mean the upward

264 fluxes and downward fluxes, respectively.

265   In the radiative transfer module, the absorption and multiple scattering

266 effects are taken into account during flux calculations by the Discrete

267 Ordinates (DISORT) approach (Nakajima and Tanaka, 1988; Stamnes et al.,

268 1988). The gaseous distributions and single fixed aerosol vertical distribution

269 (exponential to 1 km) from the multi-layered US standard 1976 atmosphere

270 were used in the radiative flux calculations (García et al., 2008). García et al.

271 (2008) pointed out that the error for the observed solar radiation at the surface

272 in global was +2.1 ± 3.0% for an overestimation of about +9 ± 12 Wm^{-2}. The

273 data used in preparing the figures for the present paper have been made

274 available as an Appendix.

275

276 **3. Results and discussion**

277 **3.1 Spatial distribution of aerosol microphysical properties**

278   A map showing the 50 CARSNET sampling sites and plots of the aerosol

279 volume size distributions (dV(r)/dlnr) at each of the sites is shown in Fig. 1.

280 Generally, the annual mean effective radius of total particles (R_{effT}) decreased

281 from the inland northwest to the southeastern coastal areas. Furthermore, the

282 volume concentration of total particles was found substantially higher at the

283 urban sites. The volume of the coarse mode particles was considerably larger

284 than that of the fine mode particles at the remotes, arid/semi-arid sites and at

285 those sites on the CLP-Chinese Loess Plateau or nearby, indicating that those

286 areas were most strongly affected by larger particles, most likely mineral dust

287 as discussed below.

288   The average (arithmetic mean) R_{effT} at the remote sites was about 0.47

289 μm with the volume about 0.05 $μm^3/μm^2$ (Table 1). A large R_{effT} (0.64 μm) was

290 found at Lhasa, and the total aerosol volume there was 0.05 $μm^3/μm^2$. These

291 results are consistent with those reports by Li et al. (2018) who found high

292 levels of coarse mode particles at Lhasa due to the presence of mineral dust.

293   The two other remote sites, Akedala and Shangri-La, had smaller average R_{effT}

294   values than Lhasa (0.36 and 0.39 µm, respectively), and corresponding

295   volumes were 0.06 and 0.03 µm^3/µm^2. The average fine-mode effective radius

296   (R_{effF}) was 0.14 µm at the remote sites, and fine-mode particle fractional

297   volume (PV_F) was 0.01 µm^3/µm^2, while the average coarse-mode effective

298   radii (R_{effC}) was 2.35 µm and the coarse-mode fractional volume (PV_C) was

299   0.03 µm^3/µm^2. These findings indicated that the contribution of coarse-mode

300   particles to the total volume of aerosol was larger at the remote sites. A study

301   by Cong et al. (2009) at the remote Nam Co site on the Tibetan Plateau

302   showed that dust particles mainly affected the site in spring, while

303   anthropogenic aerosols were prevalent in the summer.

304   The average R_{effT} at the arid and semi-arid sites (0.55 µm) was larger than

305   at the remote sites, and the total volume of aerosols at the arid/semi-arid sites

306   also was large (0.14 µm^3/µm^2), nearly three times that at the remote sites.

307   Large R_{effT} values (0.71 µm) were found at Tazhong, which is near the

308   northwestern deserts, and the aerosol volume there also was high to 0.30

309   µm^3/µm^2. Large PV_C's were found at the arid/semi-arid sites (0.05–0.27

310   µm^3/µm^2). The arithmetic mean R_{effT} (0.49 µm) at the rural sites on or near the

311   CLP had total aerosol volumes (0.15 µm^3/µm^2) similar to those at the

312   arid/semi-arid sites. These results also show a major contribution to the

313   aerosol volumes by coarse-mode particles at the sites in or near the mineral

314   dust source regions. Bi et al. (2011) similarly found that coarse particles

315   dominated the volume-size distribution at the Semi-Arid Climate and

316   Environment Observatory of Lanzhou University (SACOL) on the CLP.

317   Small R_{effT} values (0.33 µm) were found at the rural sites in eastern China,

318   and relatively high aerosol volumes were observed there (0.18 µm^3/µm^2). In

319   the Yangtze River Delta (YRD) region, the R_{effF} was large range for 0.16–0.17

320   µm, and the PV_F's were 0.12–0.13 µm^3/µm^2. At the Mt. Longfeng background

321   site in northeastern China, the total particle volume was low (0.08 µm^3/µm^2),

322   which is consistent with minimal anthropogenic influences and low aerosol

323 loadings. Compared with the other sites, the urban areas had relatively low

324 coarse mode aerosol concentrations, but small particles were plentiful—the

325 average R_{effT} was 0.37 μm and total volume was high at 0.21 μm^3/μm^2. The

326 average R_{effF} of fine-mode particles at the urban sites was 0.16 μm with a PV_F

327 of 0.10 μm^3/μm^2 while the R_{effC} was 2.22 μm and PV_C was 0.11 μm^3/μm^2.

328   The effective radii and PV_F values showed strong relationships with

329 population density and vehicle emissions at the urban sites. High volumes of

330 fine mode particles occurred at the northeastern urban site of Shenyang (R_{effT}

331 = 0.16 μm, PV_F = 0.12 μm^3/μm^2); at major cities in northern China, including

332 Shijiazhuang (R_{effT} = 0.16 μm, PV_F = 0.12 μm^3/μm^2) and Zhengzhou (R_{effT} =

333 0.18 μm, PV_F = 0.12 μm^3/μm^2); at Chengdu, a city in the Sichuan Basin of

334 (R_{effT} = 0.21 μm, PV_F = 0.16 μm^3/μm^2); and at the urban regions of Nanning

335 (R_{effT} = 0.18 μm, PV_F = 0.13 μm^3/μm^2) and Panyu (R_{effT} = 0.16 μm, PV_F = 0.10

336 μm^3/μm^2) in southern China. Overall, these results show that the volumes of

337 fine-mode particles increased at the urban sites where anthropogenic

338 influences were most apparent.

339   Cheng et al. (2015) found different aerosol volume size distributions for

340 dust and sea salt at Shanghai in the eastern China, and they showed that their

341 relative abundances varied with season and in response to local or long-range

342 transport. Zhao et al. (2018) reported the effect of sea salt aerosol on the

343 aerosol absorption and radiative effects in the coastal region over northeastern

344 China. Especially the particles hygroscopic growth with different composition

345 observed in special climatic conditions could affect aerosol microphysical

346 properties by geographically variable effects (Zhang et al., 2015; Sun et al.,

347 2010). Like in the YRD region, hygroscopic growth of fine-mode particles could

348 lead to larger AOD and scattering enhancing reported by Sun et al. (2018) and

349 Che et al. (2018). Xia et al. (2019) observed the aerosol hygroscopic growth on

350 fine particle scattering coefficient in Beijing.

351

352 **3.2 Spatial distributions of AOD and EAE**

353   The spatial distributions of $AOD_{440\text{ nm}}$ and $EAE_{440\text{-}870\text{ nm}}$ are shown in Fig. 2.

354   The AOD_{440nm} increased from the remote/rural sites to the urban sites, and as

355   one might expect, the remote sites were the least affected by particle

356   emissions and had the lowest aerosol loadings. For example, the AOD_{440nm} at

357   the remote stations was low and had an average value of 0.12. The Lhasa and

358   Shangri-La sites on the Tibetan Plateau had similar average AOD_{440nm} values

359   of 0.10. These phenomenons are similar to the study of Li et al. (2018), who

360   showed clean air conditions at Lhasa with AOD < 0.1. Cong et al. (2007, 2009)

361   also found a low AOD (0.05) at Nam Co, which was comparable to the

362   background levels at other remote sites.

363   The AOD_{440nm}'s at the arid/semi-arid sites and those on or near the Loess

364   Plateau ranged from 0.32–0.42, which is higher than at the remote sites. The

365   high AOD_{440nm} at Tazhong (0.60), which is near the deserts in northwestern

366   China was likely due to the large aerosol volume of 0.30 $\mu m^3/\mu m^2$ (section 3.1)

367   caused by mineral dust. Indeed, arid and semi-arid regions in northwestern

368   China are important sources of aeolian dust on a global scale (Bi et al., 2011).

369   Li et al. (2012) showed that the contribution of dust to the average AOD at

370   SACOL near Lanzhou was 28.4%. Other sites that showed large AOD_{440nm}

371   include regions with strong anthropogenic influences, such as Dengfeng (0.79)

372   on the North China Plain, Huimin (0.83) in the YRD (0.83 to 0.87) and Huainan

373   (0.91) in the Guanzhong Plain.

374   Compared with the sites just discussed, lower AOD_{440nm}'s were found at

375   the Mt. Longfeng background station of the Northeast China Plain (0.34), the

376   semi-arid rural site as Tongyu in northeastern China (0.23), and the clean

377   Xiyong site in southern China (0.41). Zhu et al. (2014) found a low AOD of 0.28

378   at the North China Plain regional background site. Che et al. (2009c) have

379   pointed out that the large AOD at Lin'an was likely affected by the high aerosol

380   loadings in YRD Region. Among the urban sites in China, large $AOD4_{40nm}$'s

381   were found in the cities with strong influences of anthropogenic activities, such

382   as the Northeastern Plain (Shenyang 0.89), North China Plain (Zhengzhou

383   0.99), Central China (Wuhan 1.00) and Sichuan Basin (Chengdu 1.17); the

384   average value for these sites was 0.79. Lower AOD_{440nm}'s, that is < 0.50,

385   occurred at remote sites in northwestern China, including Urumqi (0.42),

386   Yinchuan (0.37); those sites are affected less by industrial activities and the

387   population densities are lower compared with the sites in northern or eastern

388   China.

389   It is worth noting that the particle emissions in or around the urban sites

390   could lead to large optical extinctions due to hygroscopic aerosol growth,

391   especially in summer when the relative humidity is often high. In a related

392   study, Zhang et al. (2018) found a large AOD of 1.10 at Wuhan in central China

393   and that was linked to secondary aerosol formation under the high

394   summertime temperatures. Li et al. (2015) similarly concluded that high

395   temperature and humidity promoted the formation of fine particles and led to

396   hygroscopic aerosol growth at Nanjing. Qin et al. (2017) observed a high

397     $AOD_{500\ nm}$ of 1.04 at Shijiazhuang and related this to the hygroscopic growth of

398   aerosol fine-mode particles during polluted days.

399   Clear spatial variability in EAE values over China is evident in Fig. 3, and

400   at the remote sites, the average EAEs were 1.03. The EAE at Lhasa (0.77)

401   was lower than at Akedala (EAE = 1.13), which is in an arid region of central

402   Asia, or at Shangri-La (EAE = 1.19) in Tibet. The average coarse-mode

403   average effective radius (ReffC) at Lhasa was 2.26 μm and the fractional

404   volume was 0.04 $μm^3/μm^2$, this result suggests the major components of the

405   large mineral dust particles in aerosol populations over that region. The

406   smaller sphericity fraction (~42.70) and lower FMF (0.66) at Lhasa indications

407   the presence of non-spherical aerosol coarse particles compared with the

408   spherical fine particles in the urban sites.

409   At the arid and semi-arid sites in China, the average EAE value (0.71) was

410   relatively low and the FMF also was low (0.58). The EAE was extremely low at

411   Tazhong (0.25), which is in the Takliman Desert in the Xinjiang Uygur

412   Autonomous Region of northwestern China and the sphericity fraction (12.87)

and FMF (0.35) there were lower compared with most of the other sites. This finding indicates a strong contribution of large particles in this desert region consistent with large volume of the coarse-mode particles (0.27 $\mu m^3/\mu m^2$) noted in section 3.1. The average EAE reached 0.93 at the rural sites near the CLP, and the average value of FMF for those sites was 0.73. Eck et al. (2005) found especially low EAE values in March and April (0.3 and 0.4, respectively) at Yulin, China, where the dust aerosol dominated the optical column.

Large EAEs (1.23) were found at the sites in eastern China, and the FMFs also were large (0.89) at those sites. This result can be attributed to the strong impacts of anthropogenic in the more urbanized eastern part of the country. On the other hand, large EAE values also occurred at the clean sites in northeastern China, including Mt. Longfeng (1.38), where the sphericity fraction was 58.5 and the FMF 0.90. This shows that small particles can have stronger effects in these areas relative to some other regions of China. The EAE at Lin'an was larger than that at Shangdianzi in the Northern Plain or Longfengshan in Northeastern China for most months according to data from Che et al. (2009c). At the urban sites, large EAEs were found at sites in southern China, including Nanning (EAE = 1.36, sphericity fraction = 70.12, FMF = 0.95), Panyu (EAE = 1.43, sphericity fraction = 75.55, FMF = 0.93) and Zhuzilin (EAE = 1.45, sphericity fraction = 55.51, FMF = 0.94). This is likely because the large populations and widespread vehicle ownership in those cities led to the dominance of fine-mode particles throughout the year. Cheng et al. (2015) found a unimodal distribution of EAE centered in 1.1–1.6 with the occurrence frequency about 72%, which indicated an abundance of fine primary particles at Shanghai in eastern China. At the urban Nanjing site, which is in east-central China, small particles were dominant, and the annual average EAE was 1.21 ± 0.28 (Li et al., 2015).

3.3 Spatial distribution of aerosol single-scattering albedo

The spatial distribution of SSA at 440 nm of the 50 CARSNET stations is

443   shown in Fig. 4. As a frame of reference, Eck et al. (2005) reported that that

444   SSA_{440nm} from the AERONET retrievals were 0.82 to 0.98 globally. We note

445   that SSA_{440nm} values in this range reflect slightly to strongly absorbing aerosols,

446   and these particles originate from multitude sources (Che et al., 2018). The

447   SSA_{440nm}'s decreased from remote/rural to the urban sites and from west to

448   east, which means that there were higher percentages of absorbing particles

449   at the urban and eastern stations. The average SSA_{440nm} at the remote sites

450   was about 0.91, which is indicative of particles with moderate absorption. The

451   absorbing aerosols at the remote sites were more likely mineral dust particles

452   because those sites are less likely to be affected by carbonaceous particles,

453   which also are absorbing, but mainly produced by anthropogenic activities.

454   The SSA_{440nm}'s for the arid and semi-arid sites were 0.89. The relatively high

455   SSA at Tazhong (0.92) was probably due to slightly absorbing, coarse mode

456   dust particles (EAE = 0.25).

457   A study by Bi et al. (2011) showed that SSAs increased slightly with

458   wavelength when dust was present at the SACOL site. Moderately absorbing

459   particles were found in our study on or near the Chinese Loess Plateau where

460   the SSA_{440nm}'s were typically 0.88 to 0.89. Eck et al. (2005) concluded that the

461   spectral SSA demonstrated effects of dust at Yulin because the SSA increased

462   for wavelengths from 440 to 675 nm. At the rural sites in eastern China, large

463   SSA_{440nm}'s mainly occurred at sites in the YRD affected anthropogenic

464   influences; these include Tonglu (0.93), Xiaoshan (0.93), Xiyong (0.94). Che et

465   al. (2018) found the slightly absorbing particles came from industrial activity

466   and anthropogenic sources at YRD region with the $SSA_{440\ nm}$ between 0.91

467   and 0.94.

468   The average value of SSA_{440nm} at the urban sites was 0.90, which

469   indicates that particles with moderate absorption dominated the aerosol

470   populations. Cheng et al. (2015) reported a seasonal range of SSA from 0.88

471   to 0.91 at Shanghai, with higher values in autumn and winter compared with

472   spring and summer. Lower SSA_{440nm}'s occurred at the urban sites and

473   industrial regions in northeastern China, such as Shenyang (0.84), Anshan

474   (0.89), Fuhsun (0.84), which indicates that the particles were more strongly

475   absorbing in that region. On the other hand, higher SSA_{440nm}'s were found at

476   urban sites in southern China, including Nanning (0.92), Panyu (0.90) and

477   Zhuzilin (0.96), and this indicates that the particles at those sites were slightly

478   or weakly absorbing.

479   Moreover, we found that the SSA_{440nm} spatial distribution reflected the

480   percentages of absorbing aerosols at the urban sites both in northern and

481   eastern China. The reports of Dubovik et al. (2000, 2002, 2006) showed that

482   SSA values vary with both particle size and composition, and Su et al. (2017)

483   used the variations in SSA with wavelength to indicate the presence of brown

484   carbon aerosols at Tianjin, a coastal megacity in China. Qin et al. (2017)

485   suggested that the small SSAs found at Shijiazhuang indicated the presence

486   of fine-mode absorbing particles, such as brown carbon. Zhuang et al. (2014)

487   reported that the SSA at the Nanjing urban site ranged from 0.90 to 0.95, and

488   the aerosol was more absorbing in autumn, possibly due to the biomass

489   burning emission in the YRD. As evident in the results presented in section 3.1,

490   one can see that the R_{effT}, R_{effF} and R_{effC} between northeastern and southern

491   China was very similar. For example, at Shenyang, a megacity in northeastern

492   China, the effective radii of total, fine- and coarse-mode particles were 0.31,

493   0.16, 2.23 μm and the corresponding volumes were 0.22, 0.12, 0.10 $\mu m^3/\mu m^2$,

494   respectively. At Hangzhou in the YRD region, the R_{effT}, R_{effF} and R_{effC} were 0.30,

495   0.17, 2.21 μm with the volumes about 0.22, 0.12, 0.10 $\mu m^3/\mu m^2$, respectively.

496   Therefore, the different SSA_{440nm} distributions in the two regions may be

497   attributed by the special aerosol composition related to the urban-industrial

498   background of northeastern China (lower SSA_{440nm}) and more anthropogenic

499   sources in the eastern China environmental (higher SSA_{440nm}).

500   Dust aerosols with light-absorbing occur more frequently in spring in

501   northeastern China than in more southern regions (Zhao et al., 2018).

502   Anthropogenic emissions from seasonal biomass burning and residential

heating are two other main factors that affect aerosol composition between the two regions (Che et al., 2018). Especially in winter, there was high percentage of absorbing aerosols at the northeastern sites, and that was more than likely caused by emissions of carbonaceous aerosol from residential heating (Zhao et al., 2015). Climatic conditions are also the main factors affecting the absorption characteristics of aerosols in different regions of north and south China. The increased light scattering could well be due to the particles hygroscopic growth demonstrated in other studies. For example, Mai et al. (2018) found that AODs and SSAs both increased with relative humidity at Guangdong in the PRD region, which suggests that condensational growth can affect the aerosol optical properties.

3.4 Spatial distributions of absorption aerosol optical depth (AAOD)

The spatial distribution of AAOD at 440 nm shown as Fig. 5 indicates that overall, the $AAOD_{440nm}$'s increased from north to south and from remote/rural to urban sites. Lower $AAOD_{440nm}$'s were found at the remote stations, where the average value was 0.01. The $AAOD_{440nm}$ at Akedala, a remote site in northwestern China, was 0.02, and that was higher than at Shangri-La or Lhasa (0.01), both of which are on the Tibetan Plateau. The low $AAOD_{440nm}$'s throughout that region indicates that the aerosol population was not strongly absorbing. Compared with these three sites, the average $AAOD_{440nm}$'s at the arid and semi-arid sites were higher (0.03); for example, an $AAOD_{440nm}$ of 0.05was found at Tazhong, which is adjacent to the desert, and that indicates that the aerosol particles were more absorbing. As discussed in sections 3.2 and 3.3, dust aerosols likely make a significant contribution to aerosol light absorption in the areas impacted by the deserts.

The low $AAOD_{440nm}$ found at Xilinhot (0.02) was probably due to the low aerosol loadings (AOD_{440nm} = 0.21) in this region. The $AAOD_{440nm}$'s at the Mt. Gaolan and Yulin rural sites which on or around the CLP were about 0.04 and 0.03, respectively, and the particles were moderately absorbing (SSA = 0.89).

533   The large $AAOD_{440nm}$ at Datong (0.09) can be explained by the high AOD_{440nm}

534   (0.58) there. Indeed, large $AAOD_{440nm}$'s were found at rural sites in eastern

535   China, where there were high AODs and low SSAs as noted in sections 3.2

536   and 3.3. Of these sites, Dengfeng (AOD_{440nm} = 0.08) and Huimin (AOD_{440nm} =

537   0.08) are located on the North China Plain, while Huainan (AOD_{440nm} = 0.10) is

538   on the Guanzhong Plain. Lower $AAOD_{440nm}$'s, from 0.02–0.03, occurred at

539   Tongyu (0.03), which is at a semi-arid region in northeastern China, at the Mt.

540   Longfeng (0.03) regional background site on the Northeast China Plain, at the

541   Yushe rural site in northern China (0.03), and at the clean Xiyong site in the

542   PRD (0.02).

543   Several urban sites showed $AAOD_{440nm}$ values greater than 0.10; these

544   include Fushun (0.11) and Shenyang (0.14) in the northeastern China,

545   Lanzhou (0.10) in the northwestern China, and Nanjing (0.10) and Wuhan

546   (0.11) in the eastern and central China. Lower $AAOD_{440nm}$'s occurred in other

547   urban areas, such as Yinchuan ($AAOD_{440nm}$ = 0.02, AOD_{440nm} = 0.37) in the

548   northwest and Zhuzilin ($AAOD_{440nm}$ = 0.03, AOD_{440nm} = 0.66) in the PRD; both

549   of these sites had relatively low AOD_{440}'s indicating weaker anthropogenic

550   influences compared with metropolitan regions of some other areas. We note

551   that there are significant uncertainties in relating aerosol absorbing properties

552   to particle types, such as black carbon, organic matter, as well as mineral dust

553   (Russell et al., 2010; Giles et al., 2012). Nonetheless, the information

554   presented here on the spatial distribution of AAODs over China may be useful

555   for the further investigations into the relationships between light absorption and

556   particle type (Liu et al., 2017; Schuster et al., 2016a, 2016b).

557

558   **3.5 Spatial distribution of direct aerosol radiative effect at the Earth's**

559   **surface and top of the atmosphere**

560   The spatial distributions of the DAREs calculated for both the bottom and

561   top of the atmosphere are shown in Fig. 6. Overall, the DARE-BOAs increased

562   from northwest to southeast and from rural to urban sites, consistent with

563 impacts from the densely populated regions around the sites. The average

564 DARE-BOA at the remote sites was -24.40 W/m^2, and in comparison, a higher

565 DARE-BOA (-33.65 W/m^2) occurred at Akedala, which occurred on a remote

566 region of northwestern China. The AOD$_{440nm}$ at Akedala was relatively low

567 (0.17) and the SSA moderate (0.90). The moderate absorption of aerosol could

568 lead to more strong surface cooling effects with little higher DARE-BOA than

569 the other remote sites. The DARE-BOAs for Lhasa and Shangri-La were

570 -22.13 and -17.43 W/m^2, respectively. These results indicate weaker surface

571 cooling effects at the remote sites relative to other regions because the aerosol

572 loadings were relatively low, as indicated by AOD$_{440nm}$'s < 0.20.

573   The average DARE-BOTs at the arid and semi-arid sites of China were

574 about -56.43 W/m^2, and those high DARE-BOAs can be explained by the

575 moderately absorbing particles (SSA = 0.89) and large AOD$_{440nm}$'s (0.32)

576 compared with the remote sites. A large DARE-BOA (-91.20 W/m^2) occurred at

577 the Tazhong site near the northwestern deserts, and there, the high AOD (0.60)

578 and the slight absorption of mineral dust (SSA = 0.92) imply substantial surface

579 cooling. The average DARE-BOA for rural sites on the Chinese Loess Plateau

580 or surrounding was -74.67 W/m^2, and that also implies cooling at the surface.

581   Several rural sites in northern and eastern China had large DARE-BOA

582 values; these include Huimin (-111.58 W/m^2), Dengfeng (-104.78 W/m^2) and

583 Huainan (-129.17 W/m^2), and at those sites the AODs were high, from 0.80–

584 0.90, and the SSAs were ~0.89. These results show stronger surface cooling

585 effects at sites influenced by anthropogenic emissions compared with the

586 remote sites or those near the deserts. The large negative DARE-BOA values

587 (-103.28 W/m^2) at the urban sites indicate that the combination of high

588 AOD$_{440nm}$'s (0.79) and moderate SSAs (0.90) can cause significant surface

589 cooling. Indeed, anthropogenic emissions presumably led to the high

590 DARE-BOAs at urban sites, including Shenyang (-144.88 W/m^2) and Fushun

591 (-116.91 W/m^2) in the Northeastern Plain, Xi'an in the Guanzhong Plain

592 (-132.55 W/m^2), Chengdu in the Sichuan Basin (-110.42 W/m^2), Lanzhou in the

western region (-126.17 W/m^2), and Nanjing (-143.38 W/m^2) and Wuhan (-171.80 W/m^2) in the Central China. These results indicate that anthropogenic aerosols can cause significant direct radiative effects at urban sites.

The DARE-TOAs increased from north to south and from rural to urban sites, and the average DARE-TOA for the remote stations was low, about -4.79 W/m^2 (Fig. 7). The DARE-TOAs at Lhasa and Shangri-La were -5.04 W/m^2 and -8.93 W/m^2, respectively. A notably small DARE-TOA was found at Akedala (-0.42 W/m^2), indicating that the effects of the aerosol on the temperature of earth-atmosphere system there would be weak. The average DARE-TOA at the arid and semi-arid sites was -10.17 W/m^2. The large DARE-TOA found at Tazhong (-23.49 W/m^2) could represent the larger contribution of slightly absorbing mineral aerosols (SSA = 0.92) and a large AOD (0.60); this indicates more cooling at surface through the absorption and scattering solar radiation compared with the less impacted sites. This is consistent with the results for Tazhong discussed in section 3.1 which showed high volumes of coarse mode particles with large radii.

The average DARE-TOA at rural sites on the Chinese Loess Plateau or nearby was about -14.56 W/m^2. Although the SSA_{440nm} were close to Gaolan and Yulin about 0.89, the TOAs were quite different (Mt. Gaolan -20.87 W/m^2; Yulin -9.09 W/m^2) which could be due to the different AOD_{440nm} about 0.36 and 0.32, respectively. In rural eastern China, the DARE-TOA was about -32.40 W/m^2, and to put this in context, Che et al. (2018) found that DARE-TOAs of −40 W/m^2 at rural sites in the YRD region, which is indicative of a relatively strong cooling effect. Low DARE-TOAs were found at the Mt. Longfeng rural site in northeastern China (DARE-TOA = -11.34, AOD_{440nm} = 0.34, SSA = 0.89) and at the Tongyu semi-arid site in northeastern China as (DARE-TOA = -8.87, AOD_{440nm} = 0.23, SSA = 0.88) where the aerosol loadings were relatively low and the absorption was moderate.

In the urban sites at central and eastern China, the average DARE-TOA values were about -30.05 W/m^2. Higher DARE-TOAs occurred at Anshan in

the Northeastern Plain (-39.66 W/m^2), Chengdu in the Sichuan Basin (-52.21 W/m^2), Hangzhou in the YRD (-40.16 W/m^2), Jiaozuo (-39.35 W/m^2) and Zhengzhou (-46.18 W/m^2) in the North China Plain, and Zhuzilin (-40.15 W/m^2) in the PRD region. The high DARE-TOA values at these urban sites imply relatively strong cooling effects due to higher aerosol loadings in the atmosphere.

3.6 Spatial distributions of aerosol mixing properties

The spatial distribution of aerosol mixing properties (Figure 8) was obtained by using the SSA$_{440nm}$, FMF, and EAE results to classify the particles based on size and absorbing properties. In previous studies by Zheng et al. (2017) and Che et al. (2018), the particles in this study were grouped into eight types as Table 2 show. Moreover, the FMF has been provided to give the particle size information in the group of the particles.

At the remote Akedala and Lhasa sites (FMF = 0.70–0.78 and SSA$_{440nm}$ = 0.85), the percentages of mixed absorbing particles (Type V) were 35-40%, while at Shangri-la (FMF = 0.76, SSA$_{440nm}$ = 0.84), the percentage was slightly lower, 24.62%. The characteristics of the particles at these remote, high-altitude sites were probably affected by the rugged topography which would promote particle mixing. The proportion of coarse mode, mainly dust, particles with moderate to strong absorption (Group VII) was highest at the arid and semi-arid sites. The percent abundances of Group VII particles were 57.90% at Dunhuang (AE = 0.26, SSA$_{440nm}$ = 0.85, FMF = 0.43) and 58.52% at Tazhong (AE = 0.20, SSA $_{440nm}$= 0.87, FMF = 0.37), respectively. Mixed absorbing particles (Type V) and strongly absorbing dust particles (Group VII) accounted for 30 to 70% of the aerosol in the rural sites on or near the CLP. The percentages of mixed absorbing particles (Type V) at Gaolan, Yulin, and Datong were 31.98%, 45.22% and 29.04%, respectively, and the average FMFs at those sites ranged from 0.70–0.76.

The proportions of the coarse-mode aerosols with strongly absorbing in

653 Group VII were about 35.23% at Gaolan and 21.21% at Yulin, which was

654 mainly dust particles with the FMFs at those sites were 0.43 and 0.48,

655 respectively. The proportion of coarse-mode particles with strongly absorbing

656 in Group VII and coarse-mode particles with weakly-absorbing in Group VIII at

657 the rural sites in eastern China were < 11%. These patterns indicated that the

658 differences in the eastern region from northwestern China because in the east,

659 coarse-mode particles have only a minor contribution to aerosol absorption.

660 The percentage of fine-mode particles with weakly-absorbing in Type IV and

661 mixed absorbing particles in Type V combined about ~50% at the eastern sites.

662 This result suggests that mixed aerosols originated from a variety of sources

663 and that many of the sites were affected by anthropogenic emissions from

664 megacities upwind.

665 The fine-mode particles with absorbing in Types I, II, III and V accounted

666 for 50 to 90% at most of the urban sites. The percentages of these four particle

667 types combined were especially large in eastern China; for example, at Panyu,

668 particle Types I—IV composed 90.83% of the total, and the FMF there was

669 0.90–0.94, while at Zhuzilin, the percentage of Types I–IV was 92.55%, and

670 the FMF was 0.92–0.94. These results are another indication that fine-mode

671 particles are important for light absorption in urban areas. In contrast, the

672 Lanzhou and Urumqi urban sites were less affected by absorbing fine-particles

673 because the percentages of Type I–IV particles were only 19.73% and 18.36%,

674 respectively. The mixed absorbing Type V particles accounted for large

675 percentages of the total at Lanzhou (48.80%, EAE = 0.88, SSA = 0.82, FMF =

676 0.73) and at Urumqi (59.39%, EAE = 0.94, SSA = 0.84, FMF = 0.75). Different

677 from the other urban sites, these patterns show that larger particles had

678 significant contributions to the aerosol absorption at these two northwestern

679 sites.

680

681 **4. Conclusions**

682 Aerosol microphysical and its optical properties obtained from the

ground-based sunphotometer deployed at 50 CARSNET stations were used to begin the development of their climatology characteristics and to investigate potential aerosol-climate effects over vast area of China. Direct aerosol radiative effects (DAREs) at the bottom and at the top of the atmosphere were calculated, and eight types of aerosols were classified based on the particle size and absorbing properties. The annual mean values of the R_{effT} decreased from the arid and semi-arid sites (0.55 μm) to the urban sites (0.37 μm). The aerosol volumes increased from the remote sites (0.05 $μm^3/μm^2$) to the urban sites (0.21 $μm^3/μm^2$). The volumes of coarse-mode particle were larger than those for the fine mode at the remote and arid/semi-arid sites—this can be explained by the greater relative abundances of mineral dust compared with pollution-derived particles at those sites. At the urban sites, where anthropogenic influences were relatively strong, the proportion of fine mode particles increased gradually with aerosol volume.

The AOD_{440nm} progressively increased from the remote sites (0.12) to the arid and semi-arid sites (0.32) to rural sites in eastern China (0.70) and finally to the urban sites (0.79), which were the ones most strongly affected by anthropogenic activities. The average $EAE_{440-870\ nm}$'s at the arid and semi-arid sites were relatively low (0.71), which indicates an important contribution of larger particles to the aerosol extinction in those regions. The consistently large $EAE_{440-870\ nm}$'s at the urban sites (> 1.20) and the high FMFs that those sites (0.88) are the evidence that fine mode particles are prevalent throughout year. The average SSA_{440nm}'s at the remote, rural, and urban sites were relatively similar, averaging about 0.89, and this indicates the particles were moderately absorbing.

Overall, dust aerosols with light-absorbing in spring and emissions came from biomass burning and residential heating during the colder months were the main factors that led to spatial differences in the percentages of absorbing aerosols over China. The $AAOD_{440nm}$'s increased from the remote sites (0.01) to the arid and semi-arid sites (0.03) to the rural sites of eastern China (0.05)

and finally to the urban sites (0.07). High $AAOD_{440nm}$'s were caused by light-absorbing dust aerosols at the rural sites and by the strong anthropogenic emissions in the metropolitan areas. The spatial patterns in the absorbing aerosols were not only affected by the chemical composition of aerosol, but also by physical effects imposed by topography, weather, and climate.

The average DARE-BOA values were -24.40 W/m^2 at the remote sites; -56.43 W/m^2 at the arid and semi-arid sites; -74.67 W/m^2 at the sites on the CLP or nearby; -85.25 W/m^2 at the rural sites in eastern China; and -103.28 W/m^2 at the urban sites. The larger DARE-BOA values at the urban sites imply stronger cooling effects from anthropogenic emissions compared with those from mineral dust at the remote sites or those near the desert. Moreover, larger DARE-TOA's also occurred at the urban sites (-30.05 W/m^2), which indicates strong cooling effects due to the large aerosol extinctions between the earth-atmosphere system displayed the moderate to strong light absorption. Mixed-absorbing particles were the most abundant aerosol type in the remote and rural sites on or near the Chinese Loess Plateau and in eastern China. Mineral dust particles with moderate to strong absorbing were dominant in the arid and semi-arid sites while absorbing fine-mode particles accounted for 50 to 90% of the aerosol at the most urban sites.

The results of the study have considerable value for ground truthing satellite observations and for validating aerosol models. Moreover, the results also have provided significant information on aerosol optical and radiative properties for different types of sites covering a broad expanse of China. These results also are a major step towards developing climatology for aerosol microphysical and optical properties for China and even East Asia.

Data availability:

The detailed CARSNET AOD data used in the study has been deposited in the figshare database, https://figshare.com (https://doi.org/10.6084/m9.figshare.9731339.v2).

Competing interests.

743   The authors declare that they have no conflict of interest.

Author contribution:

745   All authors contributed to shaping up the ideas and reviewing the paper. HC, XX and XZ designed and implemented the research, as well as prepared the manuscript; HC, HZ,YW and HW contributed to analysis of the CARSNET dataset; HC, XX, JZ, OD, BNH, PG, and ECA contributed to the CARSNET data retrieval; HC, BQ, WG, HY, RZ, LY, JC, YZ, KG, and XZ carried out the CARSNET observations; OD, BNH, PG, and ECA provided constructive comments on this research.

Acknowledgments

753   This work was supported by grants from the National Science Fund for Distinguished Young Scholars (41825011), the National Key R & D Program Pilot Projects of China (2016YFA0601901), National Natural Science Foundation of China (41590874), the CAMS Basis Research Project (2017Z011), the European Union Seventh Framework Programme (FP7/2007-2013) under grant agreement no. 262254. AERONET-Europe ACTRIS-2 program, European Union's Horizon 2020 research and innovation programme under grant agreement No 654109.

References

Bi, J.R., Huang, J.P., Fu, Q., Wang, X., Shi, J.S., Zhang, W., Huang, Z.W., and Zhang, B.D.: Toward characterization of the aerosol optical properties over Loess Plateau of Northwestern China, Journal of Quantitative Spectroscopy and Radiative Transfer, 112, 346-360, https://doi.org/10.1016/j.jqsrt.2010.09.006, 2011.

Bokoye, A.I., Royer, A., O'Neill, N.T., Cliche, P., Fedosejevs, G., Teillet, P.M., and Mcarthur, L.J.B.: Characterization of atmospheric aerosols across Canada from a Ground-based sun photometer network: Aerocan, Atmos. Ocean., 39, 429–456, https://doi.org/10.1080/07055900.2001.9649687, 2001.

Breon, F., Tanré, D., and Generoso, S.: Aerosols effect on the cloud droplet size monitored from satellite, Science, 295, 834-838, https://doi.org/10.1126/science.1066434, 2002.

Cao, J.J., Lee, S.C., Chow, J.C., Watson, J.G., Ho, K.F., Zhang, R.J., Jin, Z.D., Shen, Z.X., Chen, G.C., Kang, Y.M., Zou, S.C., Zhang, L.Z., Qi, S.H., Dai, M.H, Cheng, Y., and Hu, K.: Spatial and seasonal distributions of carbonaceous aerosols over China, J. Geophys. Res., 112, D22S11. http://dx.doi.org/10.1029/2006JD008205, 2007.

Charlson, R. J., Schwartz, S. E., Hales, J. M., Cess, D., Coakley, J. A., and Hansen, J. E.: Climate forcing by anthropogenic aerosols, Science, 255, 423–430, https://doi.org/10.1126/science.255.5043.423, 1992.

Che, H.Z., Shi, G.Y., Zhang, X.Y., Arimoto, R., Zhao, J.Q., Xu, L., Wang, B., and Chen, Z.H.: Analysis of 40 years of solar radiation data from China, 1961-2000, Geophysical Research Letters, 32, L06803, https://doi.org/10.1029/2004GL022322, 2005.

Che, H., Shi, G., Uchiyama, A., Yamazaki, A., Chen, H., Goloub, P., and Zhang, X.: Intercomparison between aerosol optical properties by a PREDE skyradiometer and CIMEL sunphotometer over Beijing, China, Atmos. Chem. Phys., 8, 3199–3214, http://dx.doi.org/10.5194/acp-8-3199-2008, 2008.

Che, H., Zhang, X., Chen, H., Damiri, B., Goloub, P., Li, Z., Zhang, X., Wei, Y., Zhou, H., Dong, F., Li, D., and Zhou, T.: Instrument calibration and aerosol optical depth (AOD) validation of the China Aerosol Remote Sensing Network (CARSNET), J. Geophys. Res., 114, D03206, https://doi.org/10.1029/2008JD011030, 2009a.

Che, H. Z., Zhang, X. Y., Alfraro, S., Chatenet, B., Gomes, L., and Zhao, J. Q.: Aerosol optical properties and its radiative forcing over Yulin, China in 2001 and 2002, Adv. Atmos. Sci., 26, 564–576, https://doi.org/10.1007/s00376-009-0564-4, 2009b.

Che, H. Z., Yang, Z. F., Zhang, X. Y., Zhu, C. Z., Ma, Q. L., Zhou, H. G., and

Wang, P.: Study on the aerosol optical properties and their relationship with aerosol chemical compositions over three regional background stations in China, Atmospheric Environment, 43, 1093–1099, https://doi.org/10.1016/j.atmosenv.2008.11.010, 2009c.

Che, H., Xia, X., Zhu, J., Li, Z., Dubovik, O., Holben, B., Goloub, P., Chen, H., Estelles, V., Cuevas-Agulló, E., Blarel, L., Wang, H., Zhao, H., Zhang, X., Wang, Y., Sun, J., Tao, R., Zhang, X., and Shi, G.: Column aerosol optical properties and aerosol radiative forcing during a serious haze-fog month over North China Plain in 2013 based on ground-based sunphotometer measurements, Atmos. Chem. Phys., 14, 2125–2138, https://doi.org/10.5194/acp-14-2125-2014.

Che, H., Zhang, X.-Y., Xia, X., Goloub, P., Holben, B., Zhao, H., Wang, Y., Zhang, X.-C., Wang, H., Blarel, L., Damiri, B., Zhang, R., Deng, X., Ma, Y., Wang, T., Geng, F., Qi, B., Zhu, J., Yu, J., Chen, Q., and Shi, G.: Ground-based aerosol climatology of China: aerosol optical depths from the China Aerosol Remote Sensing Network (CARSNET) 2002–2013, Atmos. Chem. Phys., 15, 7619–7652, https://doi.org/10.5194/acp-15-7619-2015, 2015.

Che, H., Qi, B., Zhao, H., Xia, X., Eck, T.F., Goloub, P., Dubovik, O., Estelles, V., Cuevas-Agulló, E., Blarel, L., Wu, Y., Zhu, J., Du, R., Wang, Y., Wang, H., Gui, K., Yu, J., Zheng, Y., Sun, T., Chen, Q., Shi, G., and Zhang X.: Aerosol optical properties and direct radiative forcing based on measurements from the China Aerosol Remote Sensing Network (CARSNET) in eastern China, Atmospheric Chemistry and Physics, 18, 405–425, https://doi.org/10.5194/acp-18-405-2018, 2018.

Cong, Z.Y., Kang, S.C., Liu, X.D., and Wang, G.F.: Elemental composition of aerosol in the Nam Co region, Tibetan Plateau, during summer monsoon season, Atmospheric Environment, 41, 1180–1187, https://doi.org/10.1016/j.atmosenv.2006.09.046, 2007.

Cong, Z.Y., Kang, S.C., Smirnov, A., and Holben, B.: Aerosol optical properties

at Nam Co, a remote site in central Tibetan Plateau, Atmospheric Research, 92, 42–48, https://doi.org/10.1016/j.atmosres.2008.08.005, 2009.

Duan, J. and Mao, J.: Study on the distribution and variation trends of atmospheric aerosol optical depth over the Yangtze River Delta, Acta Scien. Circum., 27, 537–543, https://doi.org/10.1007/978-1-4020-6475-3_126, 2007.

Dubovik, O. and King, M. D.: A flexible inversion algorithm for retrieval of aerosol optical properties from sun and sky radiance measurements, J. Geophys. Res., 105, 20673–20696, https://doi.org/10.1029/2000JD900282, 2000.

Dubovik, O., Holben, B. N., Eck, T. F., Smirnov, A., Kaufman, Y. J., King, M. D., Tanre, D., and Slutsker, I.: Variability of absorption and optical properties of key aerosol types observed in worldwide locations, J. Atmos. Sci., 59, 590–608, https://doi.org/10.1175/1520-0469(2002)059<0590:VOAAOP>2.0.CO;2, 2002.

Dubovik, O., Sinyuk, A., Lapyonok, T., Holben, B. N., Mishchenko, M., Yang, P., Eck, T. F., Volten, H., Munoz, O., Veihelmann, B., van der Zande, W. J., Leon, J. F., Sorokin, M., and Slutsker, I.: Application of spheroid models to account for aerosol particle nonsphericity in remote sensing of desert dust, J. Geophys. Res.-Atmos., 111, D11208, https://doi.org/10.1029/2005JD006619, 2006.

Dubuisson, P., Buriez, J. C., and Fouquart, Y.: High spectral resolution solar radiative transfer in absorbing and scattering media, application to the satellite simulation, J. Quant. Spectrosc. Ra., 55, 103–126, https://doi.org/10.1016/0022-4073(95)00134-4, 1996.

Eck, T. F., Holben, B. N., Reid, J. S., Dubovik, O., Smirnov, A., O'Neill, N. T., Slutsker, I., and Kinne, S.: Wavelength dependence of the optical depth of biomass burning, urban, and desert dust aerosols, J. Geophys. Res., 104,

31333–31349, https://doi.org/10.1029/1999jd900923, 1999.

Eck, T. F., Holben, B. N., Dubovik, O., Smirnov, A., Goloub, P., Chen, H. B., Chatenet, B., Gomes, L., Zhang, X. Y., Tsay, S. C., Ji, Q., Giles, D., and Slutsker, I.: Columnar aerosol optical properties at AERONET sites in central eastern Asia and aerosol transport to the tropical Mid-Pacific, J. Geophys. Res., 110, D06202, https://doi.org/10.1029/2004JD005274, 2005.

Estellés, V., Campanelli, M., Utrillas, M. P., Expósito, F., and Martínez-Lozano, J. A.: Comparison of AERONET and SKYRAD4.2 inversion products retrieved from a Cimel CE318 sunphotometer, Atmos. Meas. Tech., 5, 569–579, https://doi.org/10.5194/amt-5-569-2012, 2012.

Fan, X., Chen, H., Goloub, P., Xia, X., Zhang, W., and Chatenet, B.: Analysis of column-integrated aerosol optical thickness in Beijing from AERONET observations, China Particuol., 4, 330-335, DOI: 10.1016/s1672-2515(07)60285-1, 2006.

García, O. E., Díaz, J. P., Expósito, F. J., Díaz, A. M., Dubovik, O., Dubuisson, P., Roger, J.-C., Eck, T. F., Sinyuk, A., Derimian, Y., Dutton, E. G., Schafer, J. S., Holben, B. N., and García, C. A.: Validation of AERONET estimates of atmospheric solar fluxes and aerosol radiative forcing by groundbased broadband measurements, J. Geophys. Res., 113, D21207, https://doi.org/10.1029/2008JD010211, 2008.

García, O. E., Díaz, J. P., Expósito, F. J., Díaz, A. M., Dubovik, O., and Derimian, Y.: Aerosol radiative forcing: AERONET based estimates, climate Models, InTech, edited by: Druyan, L., ISBN: 978- 953-51-0135-2, 2012.

Garrett, T. J., and Zhao, C.: Increased Arctic cloud longwave emissivity associated with pollution from mid-latitudes, Nature, 440, 787-789, doi:10.1038/nature04636, 2006.

Gelencser, A.: Carbonaceous Aerosol, Atmospheric and Oceanographic Sciences Libery., vol. 30. Springer, Netherland., 2004.

893   Giles, D. M., Holben, B. N., Tripathi, S. N., Eck, T. F., Newcomb, W. W.,

894   Slutsker, I., Dickerson, R. R., Thompson, A. M., Mattoo, S., Wang, S.,

895   Singh, R. P., Sinyuk, A., and Schafer, J. S.: Aerosol properties over the

896   Indo-Gangetic Plain: A mesoscale perspective from the TIGERZ

897   experiment, J. Geophys. Res.-Atmos., 116(D18), DOI:

898   10.1029/2011JD015809, 2011.

899   Giles, D. M., Holben, B. N., Eck, T. F., Sinyuk, A., Smirnov, A., Slutsker, I.,

900   Dickerson, R. R., Thompson, A. M., and Schafer, J. S.: An analysis of

901   AERONET aerosol absorption properties and classifications

902   representative of aerosol source regions, J. Geophys. Res.-Atmos., 117,

903   127–135, DOI: 10.1029/2012JD018127, 2012.

904   Gobbi, G. P., Kaufman, Y. J., Koren, I., and Eck, T. F.: Classification of aerosol

905   properties derived from AERONET direct sun data, Atmos. Chem. Phys.,

906   7, 453–458, http://dx.doi.org/10.5194/acp-7-453-2007, 2007

907   Goloub, P., Li, Z., Dubovik, O., Blarel, L., Podvin, T., Jankowiak, I., Lecoq, R.,

908   Deroo, C., Chatenet, B., and Morel, J. P.: PHOTONS/AERONET

909   sunphotometer network overview: description, activities, results,

910   Fourteenth International Symposium on Atmospheric and Ocean

911   Optics/Atmospheric Physics, 6936, 69360V, DOI: 10.1117/12.783171,

912   2007.

913   Haywood, J. M. and Shine, K. P.: The effect of anthropogenic sulfate and soot

914   aerosol on the clear sky planetary radiation budget, Geophys. Res. Lett.,

915   22, 603–606, https://doi.org/10.1029/95GL00075, 1995.

916   He, Q., Li, C., Geng, F., Yang, H., Li, P., Li, T., Liu, D., and Pei, Z.: Aerosol

917   optical properties retrieved from Sun photometer measurements over

918   Shanghai, China, J. Geophys. Res.-Atmos., 117, D16204,

919   https://doi.org/10.1029/2011JD017220, 2012.

920   Holben, B. N., Eck, T. F., Slutsker, I., Tanré, D., Buis, J. P., Setzer, A., Vermote,

921   E., Reagan, J. A., Kaufman, Y. J., Nakajima, T., Lavenu, F., Jankowiak, I.,

922   and Smirnov, A.: AERONET – A Federated Instrument Network and Data

Archive for Aerosol Characterization, Remote Sens. Environ., 66, 1–16, https://doi.org/10.1016/S0034-4257(98)00031-5, 1998.

Jacobson, M. Z.: A physically based treatment of elemental carbon optics: implications for global direct forcing of aerosols, Geophys. Res. Lett., 27, 217–220, DOI: 10.1029/1999gl010968, 2000.

Lacis, A. A. and Oinas, V.: A description of the correlated kdistribution method for modeling nongray gaseous absorption, thermal emission, and multiple scattering in vertically inhomogeneous atmospheres, J. Geophys. Res., 96, 9027–9063, DOI: 10.1029/90JD01945, 1991.

Lee, K. H., Li, Z., Cribb, M. C., Liu, J., Wang, L., Zheng, Y., Xia, X., Chen, H., and Li, B.: Aerosol optical depth measurements in eastern China and a new calibration method, J. Geophys. Res., 115, 4038–4044, https://doi.org/10.1029/2009JD012812, 2010.

Li, C.C., Mao, J.T., Lau, A.K.H., Chen, J.C., Yuan, Z.B., Liu, X.Y., Zhu, A.H., and Liu, G.Q.: Characteristics of distribution and seasonal variation of aerosol optical depth in eastern China with MODIS products, Chinese Science Bulletin., 48, 2488-2495, DOI: 10.1360/03wd0224, 2003.

Li, Z., Chen, H., Cribb, M., Dickerson, R., Holban, B., Li, C., Lu, D., Luo, Y., Maring, H., Shi, G., Tsay, S.C., Wang, P., Wang, Y., Xia, X., and Zhao, F.: Overview of the East Asian Studies on tropospheric aerosols, an international regional experiment(EAST-AIRE), J. Geophys. Res., 112, D22S00. http://dx.doi.org/10.1029/2007JD008853, 2007.

Li, X., and Zhang, L.: Analysis of aerosol sources and optical properties based on backward trajectory method over SACOL, Acta Physica Sin., 61, 1-9, DOI: 10.7498/aps.61.023402, 2012.

Li, Z. Q., Eck, T., Zhang, Y., Zhang, Y. H., Li, D. H., Li, L., Xu, H., Hou, W. Z., Lv, Y., Goloub, P., and Gu, X. F.: Observations of residual submicron fine aerosol particles related to cloud and fog processing during a major pollution event in Beijing, Atmos. Environ., 86, 187–192, DOI: 10.1016/j.atmosenv.2013.12.044, 2014.

Li, Z., Lau, W. K.-M., Ramanathan, V., Wu, G., Ding, Y., Manoj, M. G., Liu, J., Qian, Y., Li, J., Zhou, T., Fan, J., Rosenfeld, D., Ming, Y., Wang, Y., Huang, J., Wang, B., Xu, X., Lee, S.- S., Cribb, M., Zhang, F., Yang, X., Takemura, T., Wang, K., Xia, X., Yin, Y., Zhang, H., Guo, J., Zhai, P. M., Sugimoto, N., Babu, S. S., and Brasseur, G. P.: Aerosol and monsoon climate interactions over Asia, Rev. Geophys., 54, 866–929, https://doi.org/10.1002/2015RG000500, 2016.

Li, Z.Q., Xu, H., Li, K. T., Li, D. H., Xie, Y. S., Li, L., Zhang, Y., Gu, X.F., Zhao, W., Tian, Q.J., Deng, R.R., Su, X.L., Huang, B., Qiao, Y.L., Cui, W.Y., Hu, Y., Gong, C.L., Wang, Y.Q., Wang, X.F., Wang, J.P., Du, W.B., Pan, Z.Q., Li, Z.Z., and Bu, D.: Comprehensive Study of Optical, Physical, Chemical, and Radiative Properties of Total Columnar Atmospheric Aerosols over China: An Overview of Sun–Sky Radiometer Observation Network (SONET) Measurements, Bulletin of the American Meteorological Society., 99(4), 739–755, https://doi.org/10.1175/BAMS-D-17-0133.1, 2018.

Luo, Y., Lu, D., Zhou, X., and Li, W.: Analyses on the spatial distribution of aerosol optical depth over china in recent 30 years, Chinese Journal of Atmospheric Sciences., 26, 721-730, DOI: 10.1002/mop.10502, 2002.

Mai, B., Deng, X., Xia, X., Che, H., Guo, J., Liu, X., Zhu, J., and Ling, C.: Column-integrated aerosol optical properties of coarse- and fine-mode particles over the Pearl River Delta region in China, Sci. Total. Environ., 622–623, 481-492, DOI: 10.1016/j.scitotenv.2017.11.348, 2018.

Myhre, G.: Consistency between satellite-derived and modeled estimates of the direct aerosol effect, Science, 325, 187-190, DOI: 10.1126/science.1174461, 2009.

Nakajima, T. and Tanaka, M.: Algorithms for radiative intensity calculations in moderately thick atmospheres using a truncation approximation, J. Quant. Spectrosc. Ra., 40, 51–69, https://doi.org/10.1016/0022-4073(88)90031-3,1988.

Pappalardo, G., Amodeo, A., Apituley, A., Comeron, A., Freudenthaler, V.,

983   Linné, H., Ansmann, A., Bösenberg, J., D'Amico, G., Mattis, I., Mona, L.,
984   Wandinger, U., Amiridis, V., AladosArboledas, L., Nicolae, D., and
985   Wiegner, M.: EARLINET: towards an advanced sustainable European
986   aerosol lidar network, Atmos. Meas. Tech., 7, 2389–2409,
987   https://doi.org/10.5194/amt- 7-2389-2014, 2014.

988   Prats, N., Cachorro, V. E., Berjón, A., Toledano, C., and De Frutos, A. M.:
989   Column-integrated aerosol microphysical properties from AERONET Sun
990   photometer over southwestern Spain, Atmos. Chem. Phys., 11, 12535–
991   12547, DOI:10.5194/acp-11- 12535-2011, 2011.

992   Qin, K., Wang, L.Y., Wu, L.X., Xu, J., Rao, L.L., Letu, H., Shi, T.W., Wang, R.F.,
993   2017. A campaign for investigating aerosol optical properties during winter
994   hazes over Shijiazhuang, China, Atmos. Res., 198, 113-122,
995   https://doi.org/10.1016/j.atmosres.2017.08.018, 2017.

996   Ramanathan, V., Crutzen, P. J., Kiehl, J. T., and Rosenfeld, D.: Aerosol,
997   climate, and hydrological cycle, Science 294, 2119–2124,
998   https://doi.org/10.1126/science.1064034, 2001.

999   Remer, L. A., and Kaufman, Y. J.: Dynamic aerosol model: Urban/industrial
1000   aerosol, J. Geophys. Res., 103, 13859–13871,
1001   https://doi.org/10.1029/98jd00994, 1998.

1002   Roger, J. C., Mallet, M., Dubuisson, P., Cachier, H., Vermote, E., Dubovik, O.,
1003   and Despiau, S.: A synergetic approach for estimating the local direct
1004   aerosol forcing: applications to an urban zone during the ESCOMPTE
1005   experiment, J. Geophys. Res., 111, D13208,
1006   https://doi.org/10.1029/2005JD006361, 2006.

1007   Russell, P. B., Bergstrom, R. W., Shinozuka, Y., Clarke, A. D., DeCarlo, P. F.,
1008   Jimenez, J. L., Livingston, J. M., Redemann, J., Dubovik, O., and Strawa,
1009   A.: Absorption Angstrom Exponent in AERONET and related data as an
1010   indicator of aerosol composition, Atmos. Chem. Phys., 10, 1155–1169,
1011   https://doi.org/10.5194/acp-10-1155-2010, 2010.

1012   Shen, L., Zhao, C., Ma, Z., Li, Z., Li, J., and Wang, K.: Observed decrease of

summer sea-land breeze in Shanghai from 1994 to 2014 and its association with urbanization, Atmos. Res., doi:10.1016/j.atmosres.2019.05.007, 2019.

Shettle, E. P., and Fenn, R. W.: Models for the aerosols of the lower atmosphere and the effects of humidity variations on their optical properties. AFCRL Tech. Rep. 79 0214, Air Force Cambridge Research Laboratory, Hanscom Air Force Base, MA, 100 pp, 1979.

Stamnes, K., Tsay, S. C., Wiscombe, W., and Jayaweera, K.: Numerically stable algorithm for discrete-ordinate-method radiative transfer in multiple scattering and emitting layered media, Appl. Optics., 27, 2502–2509, https://doi.org/10.1364/ao.27.002502, 1988.

Su, X. L., Wang, Q., Li, Z. Q., Calvello, M., Esposito, F., Pavese, G., Lin, M. J., Cao, J. J., Zhou, C. Y., Li, D. H., Xu, H.: Regional transport of anthropogenic pollution and dust aerosols in spring to Tianjin — A coastal megacity in China, Sci. Total Environ., 584-585, 381-392, https://doi.org/10.1016/j.scitotenv.2017.01.016, 2017.

Sun, J. Y., Zhang, Q., Canagaratna, M. R., Zhang, Y. M., Ng, N. L., Sun, Y. L., Jayne, J. T., Zhang, X. C., Zhang, X. Y., and Worsnop, D. R.: Highly time- and size-resolved characterization of submicron aerosol particles in Beijing using an Aerodyne Aerosol Mass Spectrometer, Atmos. Environ., 44, 131–140, 2010.

Sun, T., Che, H., Qi, B., Wang, Y., Dong, Y., Xia, X., Wang, H., Gui, K., Zheng, Y., Zhao, H., Ma, Q., Du, R., and Zhang, X.: Aerosol optical characteristics and their vertical distributions under enhanced haze pollution events: effect of the regional transport of different aerosol types over eastern China, Atmos. Chem. Phys., 18, 2949–2971, https://doi.org/10.5194/acp-18-2949-2018, 2018.

Takamura, T., and Nakajima, T.: Overview of SKYNET and its activities, Opt. Pura Apl., 37, 3303–3308, 2004.

Tao, R., Che, H. Z., Chen, Q. L., Wang, Y. Q., Sun, J. Y., Zhang, X. C., Lu, S.,

1043   Guo, J. P., Wang, H., and Zhang, X.Y.: Development of an integrating

1044   sphere calibration method for Cimel sunphotometers in China aerosol

1045   remote sensing network, Particuology 13, 88–99.

1046   https://doi.org/10.1016/j.partic.2013.04.009, 2014.

1047 Twomey, S. A., Piepgrass, M., and Wolfe, T. L.: An assessment of the impact of

1048   pollution on the global cloud albedo, Tellus, 36B, 356–366,

1049   https://doi.org/10.1111/j.1600-0889.1984.tb00254.x, 1984.

1050 Wan, X., Kang, S.C., Wang, Y.S., Xin, J.Y., Liu, B., Guo, Y.H., Wen, T.X., Zhang,

1051   G.S., and Cong, Z.Y.: Size distribution of carbonaceous aerosols at a

1052   high-altitude site on the central Tibetan Plateau (Nam Co Station, 4730m

1053   a.s.l.), Atmos. Res., 153, 155–164,

1054   https://doi.org/10.1016/j.atmosres.2014.08.008, 2015.

1055 Wang, X., Huang, J.P., Ji, M.X., and Higuchi, K.: Variability of east Asia dust

1056   events and their long-term trend, Atmos. Environ., 42, 3156–3165,

1057   http://dx.doi.org/ 10.1016/j.atmosenv.2007.07.046, 2007.

1058 Wang, L. C., Gong, W., Xia, X. A., Zhu, J., Li, J., and Zhu, Z. M.: Long-term

1059   observations of aerosol optical properties at Wuhan, an urban site in

1060   Central China, Atmos. Environ., 101, 94–102, DOI:

1061   10.1016/j.atmosenv.2014.11.021, 2015.

1062 Wang, P., Che, H. Z., Zhang, X. C., Song, Q. L., Wang, Y. Q., Zhang, Z. H., Dai,

1063   X., and Yu, D. J.: Aerosol optical properties of regional background

1064   atmosphere in Northeast China, Atmos. Environ., 44, 4404–4412, DOI:

1065   10.1016/j.atmosenv.2010.07.043 , 2010.

1066 Wang, Z., Liu, D., Wang, Y., Wang, Z., and Shi, G.: Diurnal aerosol variations

1067   do affect daily averaged radiative forcing under heavy aerosol loading

1068   observed in Hefei, China, Atmos. Meas. Tech., 8, 2901–2907,

1069   https://doi.org/10.5194/amt-8-2901-2015, 2015.

1070 Wehrli, C.: Calibration of filter radiometers for the GAW Aerosol Optical Depth

1071   network at Jungfraujoch and Mauna Loa, in: Proceedings of ARJ

1072   Workshop, SANW Congress, Davos, Switzerland, 70–71, 2002.

Whitey, K. T.: The physical characteristics of sulfur aerosols. Atmos. Environ., 41(supp-S), 25-49, DOI: 10.1016/j.atmosenv.2007.10.057, 1978.

Wu, Y.F., Zhang, R.J., Pu, Y.F., Zhang, L.M., Ho, K.F., and Fu, C.B.: Aerosol optical properties observed at a semi-arid rural site in Northeastern China, Aerosol. Air. Qual. Res., 12,503–514, DOI: 10.4209/aaqr.2011.11.0202 , 2012.

Xia, C., Sun, J. Y., Qi, X. F., Shen, X. J., Zhong, J. T., Zhang, X. Y., Wang, Y. Q., Zhang, Y. M., and Hu, X. Y.: Observational study of aerosol hygroscopic growth on scattering coefficient in Beijing: A case study in March of 2018, Sci. Total Environ., 685, 239-247, 2019.

Xia, X.: A closer looking at dimming and brightening in China during 1961–2005, Ann. Geophys., 28, 1121–1132, doi:10.5194/angeo-28-1121-2010, 2010.

Xia, X., Chen, H., Goloub, P., Zong, X., Zhang, W., and Wang, P.: Climatological aspects of aerosol opticalproperties in North China Plain based on ground and satellite remote-sensing data, J. Quant. Spectrosc. Ra., 127, 12–23, DOI: 10.1016/j.jqsrt.2013.06.024, 2013.

Xie, C., Nishizawa, T., Sugimoto, N., Matsui, I., and Wang, Z.: Characteristics of aerosol optical properties in pollution and Asian dust episodes over Beijing, China. Appl. Opt., 47, 4945-4951, DOI: 10.1364/AO.47.004945, 2008.

Xie, S., Liu, X., Zhao, C., and Zhang, Y.: Sensitivity of CAM5-Simulated Arctic Clouds and Radiation to Ice Nucleation Parameterization, J. Climate., 26, 5981-5999, doi:10.1175/jcli-d-12-00517.1, 2013.

Xin, J., Wang Y, Li, Z.Q., Wang, P.C., Hao, W.M., Nordgren, B.L., Wang, S.G., Liu, G.R., Wang, L.L., Wen, T.X., Sun, Y., and Hu, B.: Aerosol optical depth (AOD) and Ångström exponent of aerosols observed by the Chinese Sun Hazemeter Network from August 2004 to September 2005, J. Geophys. Res., 112, D05203, DOI: 10.1029/2006JD007075, 2007

Xin, J.Y., Wang, L.L., Wang, Y.S., Li, Z., and Wang, P.: Trends in aerosol

optical properties over the Bohai Rim in Northeast China from 2004 to 2010, Atmos. Environ., 45, 6317–6325, DOI: 10.1016/j.atmosenv.2011.08.052, 2011.

Xin J, Wang Y, Pan Y, Ji, D., Liu, Z., Wen, T.X., Wang, Y.H., Li, X.R., Sun, Y., Sun, J., Wang, P.C., Wang, G.H., Wang, X.M., Cong, Z.Y., Song, T., Hu, B., Wang, L.L., Tang, G.Q., Gao, W.K., Guo, Y.H., Miao, H.Y., Tian, S.L., and Wang, L.: The campaign on atmospheric aerosol research network of China: CARE-China, Bulletin of the American Meteorological Society., 96, 1137-1155, https://doi.org/10.1175/BAMS-D-14-00039.1, 2015.

Yang, X., Zhao, C., Zhou, L., Li, Z., Cribb, M., and Yang, S.: Wintertime cooling and a potential connection with transported aerosols in Hong Kong during recent decades, Atmos. Res., 211, 52–61, doi:10.1016/j.atmosres.2018.04.029, 2018.

Yang, X., Zhao, C., Zhou, L., Wang, Y., and Liu, X.: Distinct impact of different types of aerosols on surface solar radiation in China, J. Geophys. Res.-Atmospheres, 121, 6459–6471. DOI: https://doi.org/10.1002/2016jd024938, 2016.

Yang, Y., Zhao, C., Dong, X., Fan, G., Zhou, Y., Wang, Y., Zhao, L., Lv, F., and Yan, F.: Toward understanding the process-level impacts of aerosols on microphysical properties of shallow cumulus cloud using aircraft observations, Atmos. Res., doi:10.1016/j.atmosres.2019.01.027, 2019.

Yang, Y., Zhao, C., Sun, L., and Wei, J.: Improved aerosol retrievals over complex regions using NPP Visible Infrared Imaging Radiometer Suite observations, Earth. Space. Sci., doi:10.1029/2019ea000574, 2019.

Yuan, Y., Shuai, Y., Li, X.W., Liu, B., and Tan, H.P.: Using a new aerosol relative optical thickness concept to identify aerosol particle species, Atmos. Res., 150, 1–11, DOI: 10.1016/j.atmosres.2014.07.007, 2014.

Zhang, L., Sun, J. Y., Shen, X. J., Zhang, Y. M., Che, H., Ma, Q. L., Zhang, Y. W., Zhang, X. Y., and Ogren, J. A.: Observations of relative humidity effects on aerosol light scattering in the Yangtze River Delta of China,

Atmos. Chem. Phys., 15, 8439-8454, https://doi.org/10.5194/acp-15-8439-2015, 2015.

Zhang, M., Ma, Y., Gong, W., Liu, B., Shi, Y., and Chen, Z.: Aerosol optical properties and radiative effects: Assessment of urban aerosols in central China using 10-year observations, Atmos. Environ., 182, 275-285, DOI: 10.1016/j.atmosenv.2018.03.040, 2018

Zhang, R., Jing, J., Tao, J., Hsu, S.-C., Wang, G., Cao, J., Lee, C.S.L., Zhu, L., Chen, Z., Zhao, Y., and Shen, Z.: Chemical characterization and source apportionment of PM2.5 in Beijing: seasonal perspective, Atmos. Chem. Phys., 13, 7053–7074, http://dx.doi.org/10.5194/acp-13-7053-2013, 2013

Zhao, C., and Garrett, T. J.: Effects of Arctic haze on surface cloud radiative forcing, Geophys. Res. Lett., 42, 557–564. doi:10.1002/2014gl062015, 2015.

Zhao, C., Lin, Y., Wu, F., Wang, Y., Li, Z., Rosenfeld, D., and Wang, Y.: Enlarging Rainfall Area of Tropical Cyclones by Atmospheric Aerosols, Geophys. Res. Lett., doi:10.1029/2018gl079427, 2018.

Zhao, C., Wang, Y., Shi, X., Zhang, D., Wang, C., Jiang, J. H., Zhang, Q., and Fan, H.: Estimating the contribution of local primary emissions to particulate pollution using high-density station observations, J. Geophys. Res.-Atmospheres, doi:10.1029/2018jd028888, 2019.

Zhao, H., Che, H., Ma, Y., Xia, X., Wang, Y., Wang, P., and Wu, X.: Temporal variability of the visibility, particulate matter mass concentration and aerosol optical properties over an urban site in Northeast China, Atmos. Res., 166, 204–212, DOI: 10.1016/j.atmosres.2015.07.003, 2015.

Zhao H., Che H., Wang Y., Wang H., Ma Y., and Wang Y.: Investigation of the Optical Properties of Aerosols over the Coastal Region at Dalian, Northeast China, Atmosphere., 7(8), 103, DOI: 10.3390/atmos7080103, 2016

Zhao, H., Che, H., Xia, X., Wang, Y., Wang, H., Wang, P., Ma, Y., Yang, H., Liu, Y., Wang, Y., Gui, K., Sun, T., Zheng, Y., and Zhang, X.: Multi-year

ground-based measurements of aerosol optical properties and direct radiative effect over different surface types in northeastern China, J. Geophys. Res.-Atmos., 123, 13,887–13,916, https://doi.org/10.1029/2018JD029141, 2018

Zhang, K., Zhao, C., Fan, H., Yang, Y., and Sun, Y.: Toward Understanding the Differences of PM2.5 Characteristics Among Five China Urban Cities, Asia-Pac. J. Atmos. Sci., doi:10.1007/s13143-019-00125-w, 2019.

Zheng, C., Zhao, C., Zhu, Y., Wang, Y., Shi, X., Wu, X., Chen, T.,Wu, F., and Qiu, Y.: Analysis of influential factors for the relationship between PM2.5 and AOD in Beijing, Atmos. Chem. Phys., 17, 13473–13489, doi: 10.5194/acp-17-13473-2017, 2017.

Zheng, Y., Che, H., Xia, X., Wang, Y., Wang, H., Wu, Y., Tao, J., Zhao, H., An, L., Li, L., Gui, K., Sun, T., Li, X., Sheng, Z., Liu, C., Yang, X., Liang, Y., Zhang, L., Kuang, X., Luo, S., and You, Y.: Five-year observation of aerosol optical properties and its radiative effects to planetary boundary layer during air pollution episodes in North China: Intercomparison of a plain site and a mountainous site in Beijing, Sci. Total. Environ., 674, 140-158, 2019.

Zhu, J., Che, H., Xia, X., Chen, H. B., Goloub, P., and Zhang, W.: Column-integrated aerosol optical and physical properties at a regional background atmosphere in North China Plain, Atmos. Environ., 84, 54–64, DOI: 10.1016/j.atmosenv.2013.11.019, 2014.

Zhuang, B., Wang, T., Li, S., Liu, J., Talbot, R., Mao, H., Yang, X., Fu, C., Yin, C., Zhu, J., Che, H., and Zhang, X.: Optical properties and radiative forcing of urban aerosols in Nanjing over China, Atmos. Environ., 83, 43–52, DOI: 10.1016/j.atmosenv.2013.10.052, 2014.

1193 **Figure captions**

1194 **Figure 1. Annual spatial distribution of aerosol volume-size distributions**

1195 **at the CARSNET sites**

1196 **Figure 2. Annual spatial distribution of aerosol optical depth (AOD) at 440**

1197 **nm at the CARSNET sites**

1198 **Figure 3. Annual spatial distribution of extinction Ångström exponent**

1199 **(AE) 440-870 nm at the CARSNET sites**

1200 **Figure 4. Annual spatial distribution of fine mode fraction at the**

1201 **CARSNET sites**

1202 **Figure 5. Annual spatial distribution of the single scattering albedo (SSA)**

1203 **at 440 nm at the CARSNET sites**

1204 **Figure 6. Annual spatial distribution of absorption aerosol optical depth**

1205 **(AAOD) at 440 nm at the CARSNET sites**

1206 **Figure 7. Annual spatial distribution of direct aerosol radiative effect at**

1207 **the bottom of the atmosphere at the CARSNET sites**

1208 **Figure 8. Annual spatial distribution of direct aerosol radiative effect at**

1209 **the top of the atmosphere at the CARSNET sites**

1210 **Figure 9. Annual spatial distribution of the aerosol type classification of**

1211 **types I–VII at the CARSNET sites**

1212 **Table 1 The aerosol type classification based on the optical properties**

1213

1214 **Figure 1. Annual spatial distribution of aerosol volume-size distributions**
1215 **at the CARSNET sites**
1216

1217
1218

Figure 2. Annual spatial distribution of aerosol optical depth (AOD) at 440 nm at the CARSNET sites
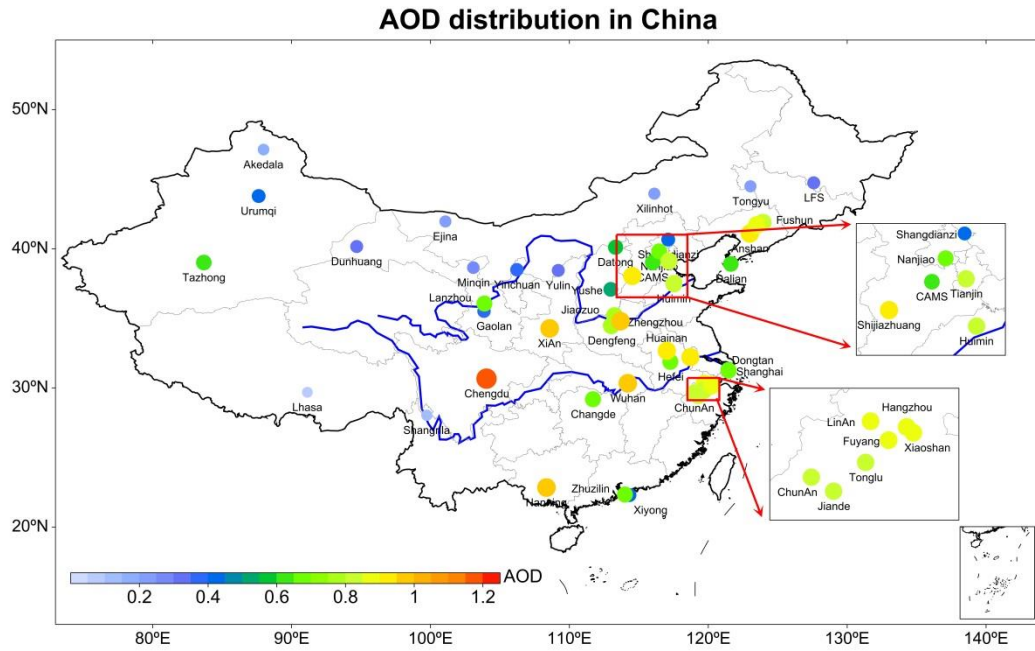
 Figure 3. Annual spatial distribution of extinction Ångström exponent
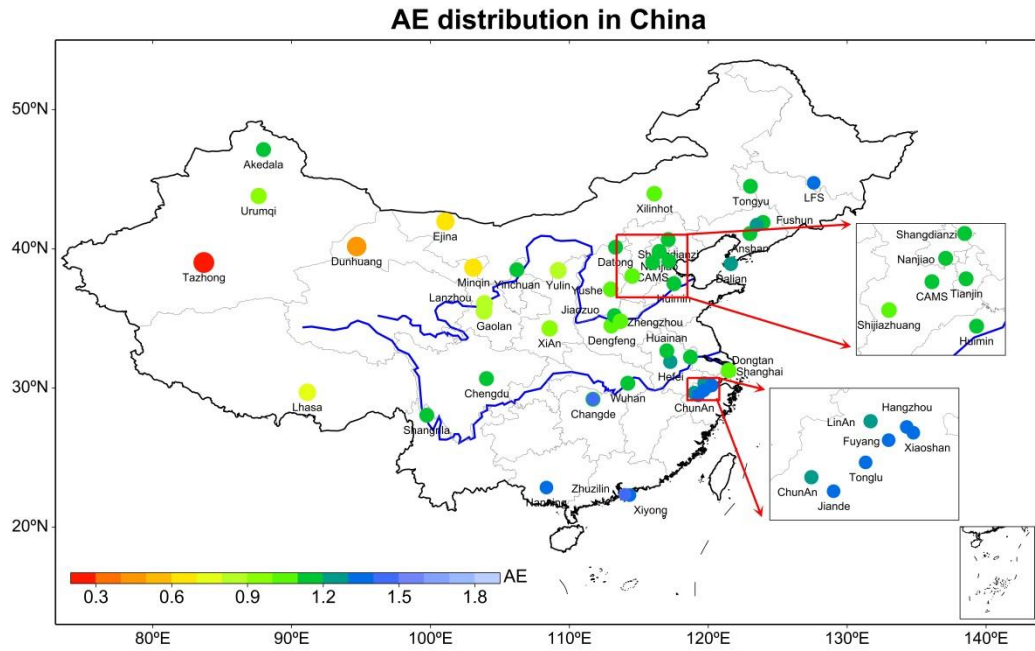
 (AE) 440-870 nm at the CARSNET sites

Figure 4. Annual spatial distribution of fine mode fraction at the CARSNET sites
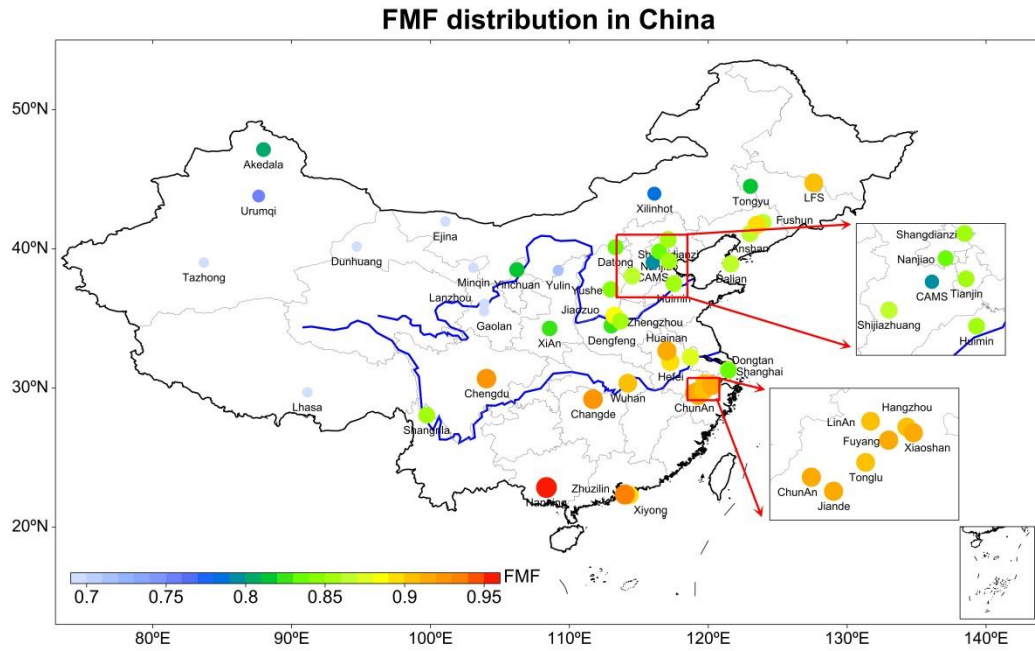
1234 **Figure 5. Annual spatial distribution of the single scattering albedo (SSA)**

1235 **at 440 nm at the CARSNET sites**

1236
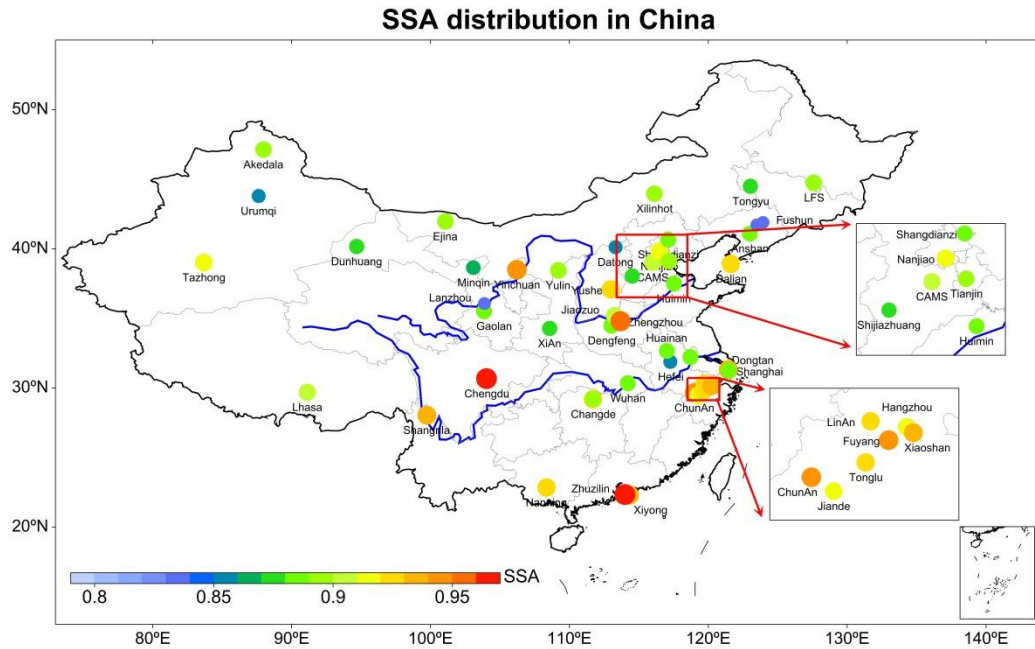
1237
1238
1239
1240

Figure 6. Annual spatial distribution of absorption aerosol optical depth (AAOD) at 440 nm at the CARSNET sites
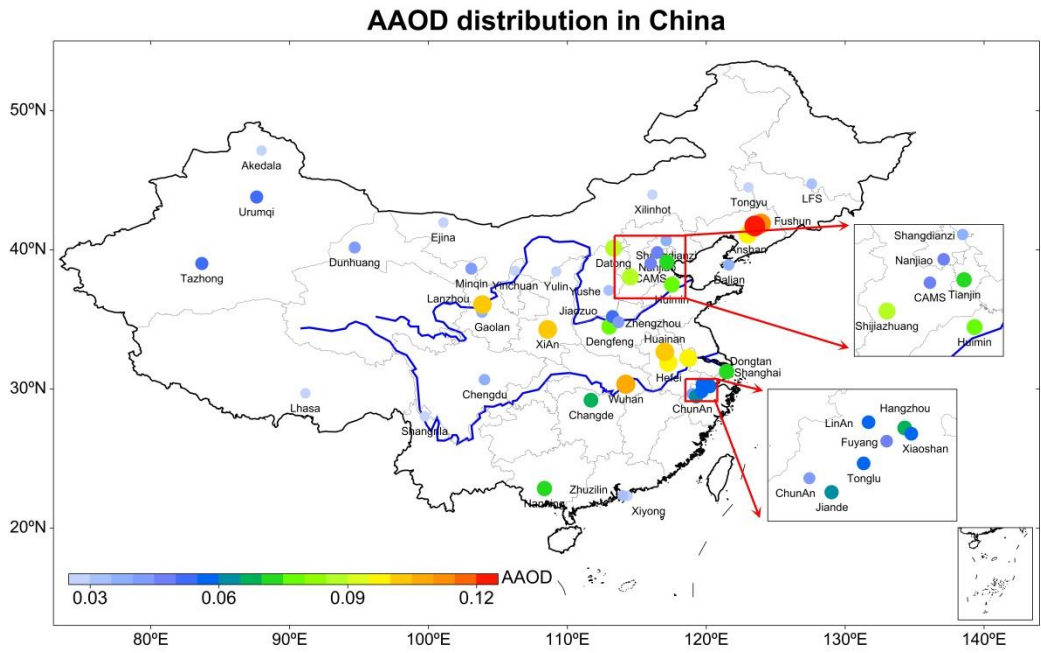
1246 **Figure 7. Annual spatial distribution of direct aerosol radiative effect at**

1247 **the bottom of the atmosphere at the CARSNET sites**

1248
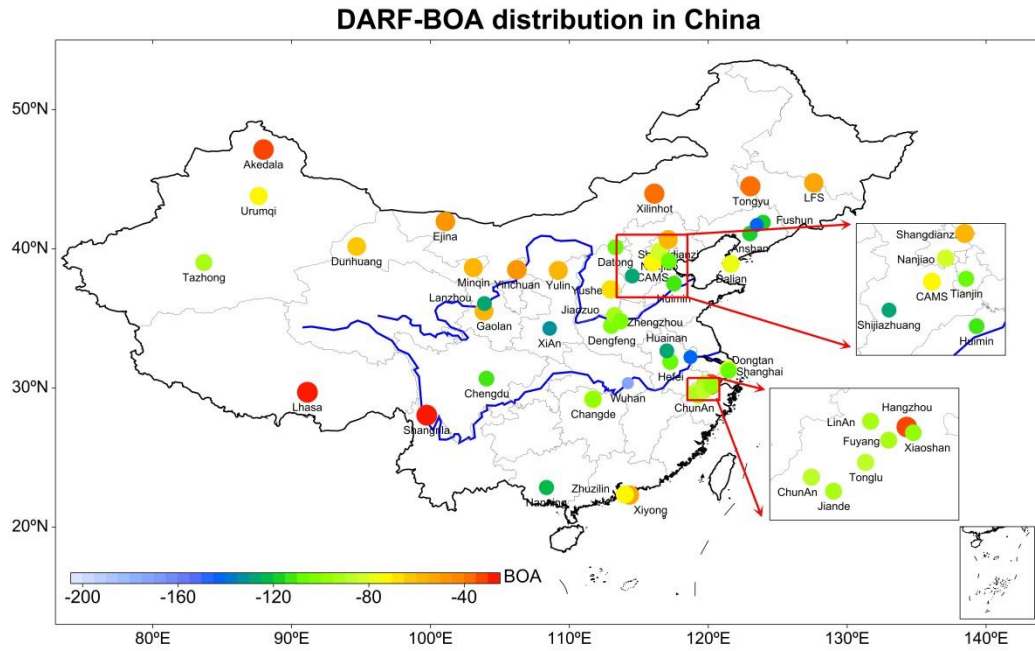
1249
1250

Figure 8. Annual spatial distribution of direct aerosol radiative effect at the top of the atmosphere at the CARSNET sites
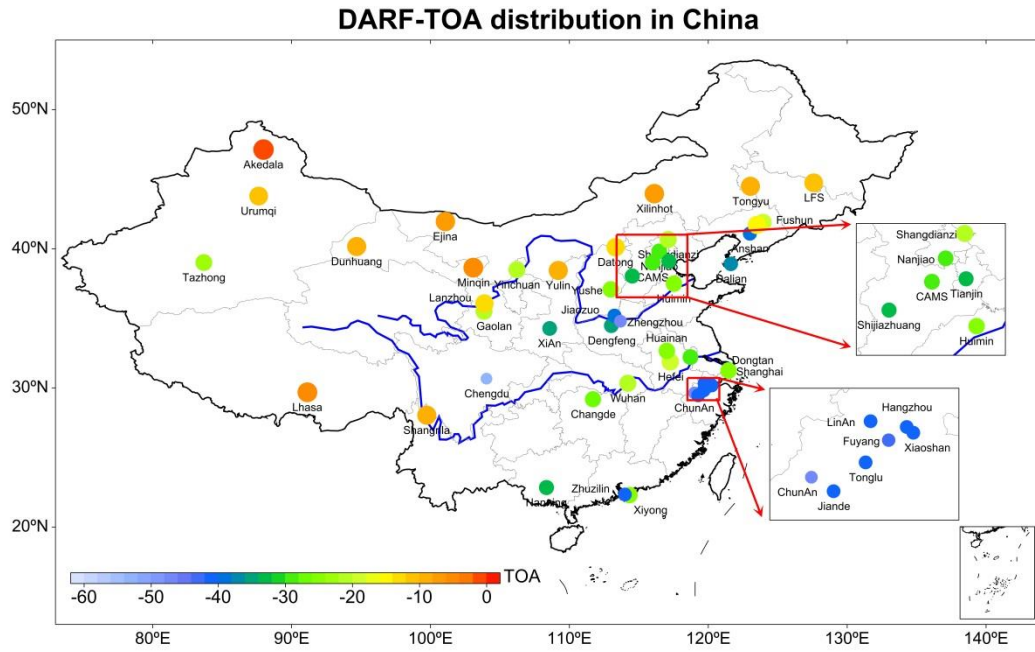
 Figure 9. Annual spatial distribution of the aerosol type classification of

 types I–VII at the CARSNET sites
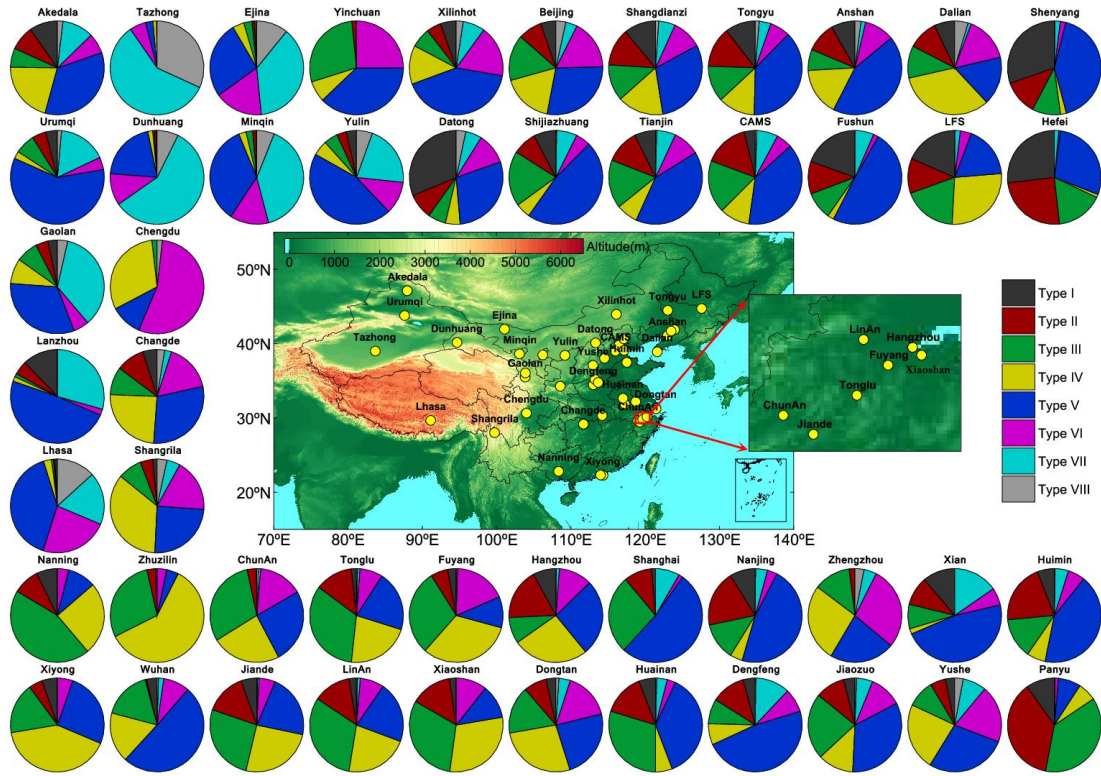
1261 **Table 1. The aerosol type classification based on the optical properties.**

1262

Type	EAE	SSA	absorbing properties and particle size
I	EAE > 1.20	$SSA_{440nm} \leqslant 0.85$	fine-mode particles with highly-absorbing
II	EAE > 1.20	$0.85 \leqslant SSA_{440nm} < 0.90$	fine-mode particles with moderately-absorbing
III	EAE > 1.20	$0.90 \leq SSA_{440nm} < 0.95$	fine-mode particles with slightly-absorbing
IV	EAE > 1.20	$SSA_{440nm} > 0.95$	fine-mode particles with weakly-absorbing
V	$0.60 \leq EAE < 1.20$	$SSA_{440nm} \leq 0.95$	mixed-absorbing particles
VI	$0.60 \leq EAE < 1.20$	$SSA_{440nm} > 0.95$	mixed-slightly absorbing particles
VII	$EAE \leq 0.60$	$SSA_{440nm} \leq 0.95$	coarse mode particles with strongly absorbing (mainly dust)
VIII	$AE \leq 0.60$	$SSA_{440nm} > 0.95$	coarse-mode particles with weakly-absorbing

1263

1264

1265

1266

1267

1268

1269

1270

1271

1272

1273

1274

1275

1276

1277

1278

1279

 Appendix

 Table 1. Site information for the 50 CARSNET sites used in this study

1282

No.	Site Name	Long.	Lat.	Alt.	Site information	Obs. Num	Period
					Remote sites (three sites)		
1	Akedala	47.12	87.97	562.0	55 km west of Fuhai county, Xinjiang province, and 250–300 km southeast of Kazakestan.	947	2010-2017
2	Lhasa	29.67	91.13	3663.0	In the center of Lhasa city, Qinghai-Xizang Plateau.	437	2012-2017
3	Shangri-La	28.02	99.73	3583.0	12 km northeast of Shangri-La county, Diqing area, Yunnan province	325	2013-2017
					Arid and semi-arid sites (six sites)		
4	Dunhuang	40.15	94.68	1139.0	1.5 km northeast of Dunhuang city, Gansu province; near Kumutage Desert of China	2030	2012-2017
5	Ejina	41.95	101.07	940.5	West ofIner-Mongolia Province, near Mongolia and Badanjilin desert	1970	2013-2017
6	Minqin	38.63	103.08	1367.0	In Minqin county, east to Tenggeli desert and north to Badanjilin Desert, Gansu Province	481	2013-2017
7	Tazhong	39.00	83.67	1099.4	In the middle of Takilamakan Desert, Xinjiang Province	1279	2013-2017
8	Xilinhot	43.95	116.12	1003.0	5 km southeast of Xilinhot City, near Hunshandake sand-land, Inner-Mongolia Province,	1464	2013-2017
9	Tongyu	44.42	122.87	151.0	In Tonyu city, west of Jilin Province	817	2010-2011
					Rural sites on the Chinese Loess Plateau or nearby (three sites)		
10	Mt.Gaolan	36.00	103.85	2161.6	5 km north of Lanzhou city in Gansu province	769	2015-2016
11	Yulin	38.43	109.20	1135.0	10 km north of Yulin city in Shaanxi province	716	2010-2016
12	Datong	40.10	113.33	1067.3	9 km of Datong City, but within area of rapid urbanization, Shanxi Province	914	2014-2017
					Rural sites in eastern China (15 sites)		
13	Changde	29.17	111.70	565.0	18 km northwest from Changde city, Hunan province.	344	2013-2016
14	Dongtan	31.52	121.96	10.0	In the Chongmin Island, 30km east of Shanghai city	986	2012-2016
15	ChunAn	29.61	119.05	171.4	151 km southwest from Hangzhou city, Zhejiang province.	1286	2011-2015
16	Huimin	37.48	117.53	11.7	100 km Northeast of Jinan City, Shandong Province	2243	2009-2017
17	Lin'an	30.30	119.73	138.6	150 km northeast of Shanghai, and 50 km west of Hangzhou city, Zhejiang province	1834	2011-2015
18	Mt.Longfeng	44.73	127.60	330.5	In Wuchang county, 175 km northeast of Harbin city, Heilongjiang Province	1515	2012-2016
19	Fuyang	30.07	119.95	17.0	44.1 km southwest from Hangzhou city, Zhejiang province.	710	2014-2015
20	Shangdianzi	40.65	117.12	293.0	In Miyun county, 150 km northeast to Beijing city.	1520	2014-2017
21	Yushe	37.07	112.98	1041.5	1.5 km east of Yushe city in Shanxi Province	1479	2013-2017
22	Dengfeng	34.46	113.02	350.0	75 km Southwest of Zhengzhou City, Henan Province	712	2013
23	Huainan	32.65	117.02	52.0	In the central of Hefei City, Anhui Province	794	2014-2015
24	Jiande	29.45	119.28	89.0	In the southwest from Hangzhou city, Zhejiang province.	1550	2011-2015
25	Tonglu	29.80	119.64	46.1	100 km northwest from Hangzhou city, Zhejiang province.	1717	2011-2015
26	Xiaoshan	30.16	120.25	14.0	In the south of Hangzhou city, Zhejiang province.	600	2014-2015
27	Xiyong	22.28	114.33	155.2	In the eastern of Shenzhen city, Guangdong province.	189	2016
					Urban sites (23 sites)		
28	Anshan	41.08	123.00	23.0	In Anshan city, central Liaoning province	193	2009-2013
29	Beijing-Nanjiao	39.80	116.47	31.3	In the southeast Beijing at city margin	1732	2014-2017
30	Beijing-CAMS	39.93	116.32	106.0	Chinese Academy of Meteorological Sciences in Beijing	1113	2012-2018
31	Chengdu	30.65	104.03	496.0	In Chengdu city, Sichuan province.	55	2014-2015
32	Dalian	38.90	121.63	91.5	Southeast coastal city in Liaoning Province	736	2012-2015
33	Fushun	41.88	123.95	80.0	In Fushun city, central Liaoning province.	231	2009-2013
34	Hangzhou	30.23	120.17	42.0	In Hangzhou city, Zhengjiang province.	1663	2011-2015

35	Hefei	31.98	116.38	92.0	In Hefei city, Anhui province.	197	2016
36	Jiaozuo	35.18	113.25	113.0	In the center of Jiaozuo city, Henan province.	981	2016-2017
37	Lanzhou	36.05	103.88	1517.3	In Lanzhou city, Gansu province.	1493	2013-2017
38	Nanjing	32.05	118.77	99.3	In Nanjing city, Jiangsu province	1258	2007-2015
39	Nanning	22.82	108.35	172.0	In Nanning city, Guangxi province	286	2013-2017
40	Panyu	23	113.35	145.0	In district of Guangzhou city, Guangdong Province	436	2012-2016
41	Shanghai	31.22	121.55	14.0	In Pudong district of Shanghai city	144	2016
42	Shenyang	41.77	123.50	60.0	In Shenyang city, central Liaoning province.	541	2009-2013
43	Tianjin	39.10	117.17	3.3	Northern coastal city in North China Plain	1705	2013-2017
44	Urumqi	43.78	87.62	935.0	In Urumuqi city, Xijiang province	1411	2012-2017
45	Xi'an	34.43	108.97	363.0	20 km north of center of Xian city, but within Jing RiverIndustrial District, Shaanxi province	652	2012-2016
46	Yinchuan	38.48	106.22	1111.5	In Yinchuan city, Ningxia province.	124	2017
47	Zhengzhou	34.78	113.68	99.0	In Zhengzhou city, Henan province.	1485	2013-2017
48	Shijiazhuang	38.03	114.53	75.0	In the center of Shijiazhuang city, Hebei province.	1178	2015-2017
49	Wuhan	30.32	114.21	30	In the center of Wuhan city, Hubei province	220	2008
50	Zhuzilin	22.32	114.00	63.0	In the central of Shenzhen city, Guangdong province.	915	2010-2017

1283

1284

1285

1286

1287

1288

1289

1290

1291

1292

1293

1294

1295

1296

1297

1298

1299

1300

1301

1302

1303

1304

1305

 Table 2. Annual data for aerosol microphysical properties, optical and direct radiative parameters

No.	Site	[a]ReffT	[a]ReffF	[a]ReffC	[a]VolT	[a]VolF	[a]VolC	[a]AODt	[b]Alpha	[a]FMF	[a]SSAT	[a]Image	[a]Real	[a]AAOD	[a]BOA	[a]TOA
							Remote sites (3 sites)									
1	Akedala	0.36	0.14	2.45	0.06	0.02	0.04	0.17	1.13	0.81	0.90	0.0117	1.4540	0.02	-33.65	-0.42
2	Lhasa	0.64	0.13	2.26	0.05	0.01	0.04	0.10	0.77	0.66	0.90	0.0106	1.5541	0.01	-22.13	-5.04
3	Shangri-La	0.39	0.14	2.33	0.03	0.01	0.02	0.10	1.19	0.85	0.93	0.0086	1.4626	0.01	-17.43	-8.93
	Average	0.47	0.14	2.35	0.05	0.01	0.03	0.12	1.03	0.77	0.91	0.0103	1.4902	0.01	-24.40	-4.79
							Arid and semi-arid sites (6 sites)									
4	Dunhuang	0.62	0.14	1.52	0.15	0.02	0.13	0.33	0.48	0.44	0.88	0.0103	1.5491	0.04	-63.61	-8.96
5	Ejina	0.56	0.14	1.78	0.11	0.02	0.09	0.24	0.64	0.52	0.89	0.0116	1.5265	0.03	-47.66	-7.20
6	Minqin	0.56	0.13	1.87	0.13	0.02	0.11	0.30	0.68	0.59	0.86	0.0145	1.5430	0.04	-59.83	-5.01
7	Tazhong	0.71	0.14	1.38	0.30	0.03	0.27	0.60	0.25	0.35	0.92	0.0054	1.5257	0.05	-91.20	-23.49
8	Xilinhot	0.48	0.13	2.45	0.08	0.02	0.05	0.21	1.03	0.78	0.89	0.0139	1.5183	0.02	-37.14	-7.47
9	Tongyu	0.39	0.13	2.36	0.07	0.02	0.05	0.23	1.16	0.82	0.88	0.0179	1.5377	0.03	-39.13	-8.87
	Average	0.55	0.14	1.89	0.14	0.02	0.12	0.32	0.71	0.58	0.89	0.0123	1.5334	0.03	-56.43	-10.17
							Rural sites on the Chinese Loess Plateau or nearby (3 sites)									
10	Mt.Gaolan	0.58	0.14	2.03	0.16	0.03	0.13	0.36	0.81	0.64	0.89	0.0108	1.5154	0.04	-59.36	-20.87
11	Yulin	0.53	0.15	2.05	0.11	0.03	0.08	0.32	0.84	0.72	0.89	0.0122	1.5070	0.03	-56.81	-9.09
12	Datong	0.35	0.13	2.15	0.19	0.09	0.10	0.58	1.15	0.83	0.86	0.0171	1.4905	0.09	-107.86	-13.71
	Average	0.49	0.14	2.08	0.15	0.05	0.10	0.42	0.93	0.73	0.88	0.0134	1.5043	0.05	-74.67	-14.56
							Rural sites in eastern China (15 sites)									
13	Changde	0.32	0.16	2.18	0.14	0.07	0.07	0.58	1.15	0.88	0.93	0.0101	1.4619	0.04	-75.33	-31.44
14	Dongtan	0.37	0.16	2.12	0.17	0.08	0.09	0.62	1.21	0.86	0.93	0.0080	1.4624	0.04	-79.41	-33.18
15	ChunAn	0.30	0.18	2.30	0.19	0.12	0.08	0.81	1.22	0.92	0.94	0.0066	1.4095	0.04	-86.49	-46.48
16	Huimin	0.36	0.15	2.07	0.22	0.10	0.12	0.83	1.14	0.86	0.89	0.0147	1.4852	0.08	-111.58	-25.49

17	Lin'an	0.29	0.17	2.24	0.21	0.12	0.09	0.87	1.29	0.91	0.93	0.0089	1.4172	0.06	-93.09	-41.73
18	Mt.Longfeng	0.28	0.15	2.44	0.08	0.04	0.04	0.34	1.38	0.90	0.89	0.0165	1.4647	0.03	-51.17	-11.34
19	Fuyang	0.29	0.17	2.28	0.21	0.13	0.09	0.89	1.31	0.92	0.94	0.0070	1.4147	0.05	-91.69	-42.29
20	Shangdianzi	0.40	0.15	2.33	0.12	0.05	0.07	0.43	1.17	0.86	0.89	0.0148	1.4840	0.04	-59.99	-20.58
21	Yushe	0.41	0.15	2.18	0.14	0.06	0.08	0.50	1.07	0.84	0.92	0.0090	1.4878	0.03	-66.72	-25.99
22	Dengfeng	0.39	0.15	2.03	0.23	0.09	0.13	0.79	1.02	0.83	0.89	0.0131	1.4782	0.08	-104.78	-35.84
23	Huainan	0.30	0.17	2.25	0.21	0.13	0.08	0.91	1.17	0.92	0.88	0.0166	1.4308	0.10	-129.17	-24.44
24	Jiande	0.29	0.17	2.18	0.20	0.12	0.08	0.84	1.34	0.91	0.92	0.0099	1.4085	0.06	-91.06	-40.07
25	Tonglu	0.29	0.17	2.20	0.20	0.12	0.08	0.83	1.31	0.91	0.93	0.0091	1.4269	0.06	-89.82	-41.28
26	Xiaoshan	0.28	0.17	2.24	0.22	0.13	0.09	0.87	1.35	0.91	0.93	0.0082	1.4134	0.06	-95.23	-40.39
27	Xiyong	0.33	0.16	2.43	0.11	0.06	0.05	0.41	1.32	0.89	0.94	0.0074	1.4072	0.02	-53.18	-25.45
	Average	0.33	0.16	2.23	0.18	0.09	0.08	0.70	1.23	0.89	0.92	0.0107	1.4435	0.05	-85.25	-32.40
	Urban sites (23 sites)															
28	Anshan	0.36	0.17	2.24	0.26	0.12	0.14	0.94	1.12	0.86	0.89	0.0158	1.4759	0.10	-117.99	-39.66
29	Beijing-Nanjiao	0.45	0.15	2.33	0.19	0.07	0.12	0.65	1.12	0.84	0.92	0.0100	1.4939	0.05	-82.06	-29.43
30	Beijing-CAMS	0.50	0.16	2.37	0.19	0.07	0.12	0.65	1.12	0.79	0.90	0.0115	1.5108	0.05	-72.66	-29.10
31	Chengdu	0.34	0.21	2.26	0.26	0.16	0.10	1.17	1.12	0.92	0.97	0.0033	1.4116	0.04	-110.42	-52.21
32	Dalian	0.35	0.16	2.24	0.16	0.08	0.09	0.62	1.22	0.87	0.93	0.0095	1.4584	0.04	-75.50	-37.42
33	Fushun	0.38	0.17	2.34	0.22	0.09	0.12	0.80	1.12	0.87	0.84	0.0244	1.4954	0.11	-116.91	-19.59
34	Hangzhou	0.30	0.17	2.21	0.22	0.12	0.10	0.87	1.30	0.90	0.91	0.0109	1.4337	0.07	-31.57	-40.16
35	Hefei	0.29	0.15	2.37	0.18	0.10	0.08	0.69	1.28	0.90	0.85	0.0195	1.4253	0.10	-105.83	-19.22
36	Jiaozuo	0.35	0.16	2.17	0.20	0.10	0.10	0.76	1.14	0.88	0.91	0.0105	1.4722	0.05	-92.29	-39.35
37	Lanzhou	0.54	0.14	2.04	0.28	0.06	0.22	0.66	0.81	0.66	0.83	0.0197	1.5193	0.10	-126.17	-13.81
38	Nanjing	0.33	0.16	2.16	0.25	0.12	0.12	0.94	1.13	0.88	0.88	0.0154	1.4446	0.10	-143.38	-28.29
39	Nanning	0.30	0.18	2.53	0.20	0.13	0.06	0.97	1.36	0.95	0.92	0.0107	1.4272	0.07	-121.92	-33.35
40	Panyu	0.26	0.16	2.29	0.16	0.10	0.06	0.69	1.43	0.93	0.90	0.0137	1.4155	0.07	-96.03	-26.56

41	Shanghai	0.40	0.15	1.93	0.19	0.08	0.11	0.68	1.10	0.84	0.88	0.0142	1.4814	0.07	-106.89	-24.34
42	Shenyang	0.31	0.16	2.23	0.22	0.12	0.10	0.89	1.20	0.90	0.84	0.0253	1.4589	0.14	-144.88	-15.02
43	Tianjin	0.42	0.16	2.26	0.23	0.10	0.13	0.83	1.11	0.86	0.89	0.0134	1.4957	0.07	-108.09	-33.26
44	Urumqi	0.48	0.14	2.14	0.15	0.04	0.10	0.42	0.93	0.75	0.85	0.0192	1.5371	0.05	-70.55	-11.74
45	Xi'an	0.37	0.16	1.85	0.26	0.11	0.15	0.98	0.98	0.82	0.88	0.0150	1.4888	0.10	-132.55	-35.93
46	Yinchuan	0.38	0.14	2.02	0.11	0.04	0.07	0.37	1.12	0.81	0.94	0.0054	1.4930	0.02	-48.67	-21.89
47	Zhengzhou	0.43	0.18	2.22	0.28	0.12	0.16	0.99	1.10	0.86	0.95	0.0045	1.4626	0.04	-101.10	-46.18
48	Shijiazhuang	0.40	0.16	2.28	0.26	0.12	0.14	0.95	1.09	0.87	0.88	0.0154	1.4754	0.09	-125.05	-33.66
49	Wuhan	0.34	0.17	2.22	0.22	0.12	0.10	1.00	1.16	0.91	0.88	0.0196	1.4779	0.11	-171.80	-20.40
50	Zhuzilin	0.27	0.17	2.45	0.15	0.09	0.05	0.66	1.45	0.94	0.96	0.0049	1.4438	0.03	-73.16	-40.65
	Average	0.37	0.16	2.22	0.21	0.10	0.11	0.79	1.15	0.86	0.90	0.0136	1.4695	0.07	-103.28	-30.05

[a] Optical parameters at a wavelength of 440 nm.

[b] Angström exponents between 440 and 870 nm.